

**SpiderNets: Estimating Fear Ratings of Spider-Related Images with Vision
Models**

Dominik Pegler¹, David Steyr¹, Mengfan Zhang¹, Alexander Karner¹, Jozsef Arato², Frank
Scharnowski¹, and Filip Melinscak¹

¹Department of Cognition, Emotion, and Methods in Psychology, Faculty of Psychology,
University of Vienna

²Vienna Cognitive Science Hub, University of Vienna

Author Note

Corresponding author: Dominik Pegler. E-mail: dominik.pegler@univie.ac.at

Abstract

Advances in computer vision have opened new avenues for clinical applications, particularly in computerized exposure therapy where visual stimuli can be dynamically adjusted based on patient responses. As a critical step toward such adaptive systems, we investigated whether pretrained computer vision models can accurately predict fear levels from spider-related images. We adapted three diverse models using transfer learning to predict human fear ratings (on a 0–100 scale) from a standardized dataset of 313 images. The models were evaluated using cross-validation, achieving an average mean absolute error (MAE) between 10.1 and 11.0. Our learning curve analysis revealed that reducing the dataset size significantly harmed performance, though further increases yielded no substantial gains. Explainability assessments showed the models' predictions were based on spider-related features. A category-wise error analysis further identified visual conditions associated with higher errors (e.g., distant views and artificial/painted spiders). These findings demonstrate the potential of explainable computer vision models in predicting fear ratings, highlighting the importance of both model explainability and a sufficient dataset size for developing effective emotion-aware therapeutic technologies.

Keywords: Specific Phobias, Computer Vision, Exposure Therapy

SpiderNets: Estimating Fear Ratings of Spider-Related Images with Vision Models

Introduction

The digitalization of healthcare, particularly in the mental health sector, is providing new possibilities for the treatment and evaluation of emotions. In specific phobias, a prevalent class of anxiety disorders, exposure therapy remains the gold standard for treatment (Choy et al., 2007; Craske et al., 2014; Davey, 2007; Healey et al., 2017), yet traditional delivery is limited by accessibility and scalability. Digital therapies promise more personalized and dynamic treatment, but they require reliable, scalable ways to quantify responses to phobia-relevant stimuli. Computer vision, a field that enables computers to understand and interpret visual data, offers tools to estimate expected fear elicited by image content. The ultimate clinical need is adaptive therapies that monitor an individual’s momentary fear state in real time; a step toward that goal is to model image-level average fear across individuals and use such predictors to guide stimulus selection.

While computer vision research has extensively explored general emotion and sentiment analysis from images (Kim et al., 2018; Sun et al., 2016; You et al., 2015), these studies rarely focus on phobia-specific stimuli or incorporate explainable AI (XAI; Barredo Arrieta et al., 2020) methods to understand how models arrive at their predictions. A key concern is that while these models may produce accurate predictions, their reasoning may not be anchored in the same visual cues that would be relevant for a human observer (Russell, 2020). Furthermore, the limited use of XAI in this context makes it difficult to trust and apply these models in a clinical setting, in contrast to some medical image analysis studies (van der Velden et al., 2022).

To address this gap, we adapted three pretrained, moderately sized vision backbones—ResNet50 (He et al., 2015), ConvNeXtV2 Tiny (Woo et al., 2023), and Swin Tiny Patch4 Window7 (Liu et al., 2021)—and fine-tuned them on a specialized dataset of

spider images to predict human fear ratings (Karner, Zhang, et al., 2024). For brevity, we refer to these as ResNet, ConvNeXtV2, and Swin. We selected these models based on their architectural differences and suitability for a clinical context, prioritizing those of moderate size with available pretrained weights. This approach, known as transfer learning (Yosinski et al., 2014), adapts models trained on large, general datasets (J. Deng et al., 2009) to new, specific tasks. We then used two XAI techniques—Grad-CAM (Selvaraju et al., 2020) and feature visualization (FV) for ResNet, reported in the Appendix (Olah et al., 2017)—to assess whether model predictions relied on image features aligned with human visual attention and clinical understanding of phobic responses. Our goal was to establish a robust and interpretable system for fear estimation from images.

This study makes three key contributions. First, we demonstrate that pretrained computer vision models can effectively learn to predict fear ratings for phobia-specific stimuli. Second, our explainability analyses help assess whether model predictions rely on clinically interpretable image cues. Beyond aggregate accuracy, identifying when and why models err is essential for interpretability, dataset curation, and clinical deployment. Therefore, our final and third contribution is a category-wise error analysis using the 12-criterion taxonomy of Karner, Obenaus, et al. (2024), which quantifies category difficulty and each category’s contribution to the total absolute error.

Methods

Data

The dataset used in our study was originally collected by Karner, Zhang, et al. (2024) and consists of fear ratings for 313 diverse spider-related images. These images range from depictions with one or more spiders, to scenes with no spiders but only cobwebs, in various contexts including nature, human contact, human environments, as well as artificial and drawn spiders. A total of 152 spider-fearful adults completed 95 trials, each involving the rating of a single image. Within each participant’s rating session, a subset of images was repeated to assess within-participant reliability. Consequently, the

number of rated unique images varied, with a mean of 91.39 unique images per participant ($SD = 1.72$, range: 87–95). In line with Karner, Obenaus, et al. (2024), we only used the rating from the first trial of each image, yielding a total of 13,891 ratings. Furthermore, each image was rated by varying numbers of participants, with a mean of 44.38 ratings per image ($SD = 12.64$, range: 24–88).

To identify and remove participant outliers, we employed a combined approach with two complementary methods. First, we used a correlation-based method to assess the agreement of individual participants with the group consensus. A consensus vector was computed to represent the median rating per item across all raters. For each participant, we extracted their vector of ratings and calculated the Spearman correlation coefficient between their ratings and the consensus vector. Participants with a correlation coefficient below the threshold defined as the first quartile (Q1) minus 1.5 times the interquartile range (IQR) of all correlation coefficients were flagged as outliers, as their rating patterns substantially deviated from the group consensus. In addition to the correlation-based method, we implemented an approach based on the median absolute deviation (Leys et al., 2013). We calculated the median rating for each image and then determined the absolute deviations of individual ratings from these medians. By computing the median absolute deviation for each participant, we identified those with deviations greater than the threshold defined as the third quartile (Q3) plus 1.5 times the IQR. This threshold indicates substantial absolute deviation of their ratings compared to the consensus rating. We identified and excluded 4 outlying participants from our dataset that contributed a total of 359 ratings. Therefore, the remaining dataset contained 13,532 ratings for 313 images from 148 raters. The overall mean fear rating across images was 50.30 ($SD = 18.98$, range: 1.82–83.15). The distributions are illustrated in the Appendix (Figure A1).

Base Models and Training

The computer vision models used in this study as our *base models* (pretrained networks used as starting points for transfer learning) were ResNet50 (He et al., 2015),

ConvNeXtV2 Tiny (Woo et al., 2023), and Swin Tiny Patch4 Window7 (Liu et al., 2021), chosen for their diverse architectural approaches and promising performance in image classification tasks. ResNet50 is a widely used convolutional neural network (CNN; LeCun et al., 2015) that has demonstrated robust performance across various applications, including adaptation for regression problems and learning latent variables Sanders and Nosofsky (2020). ConvNeXtV2 represents a newer CNN architecture, having shown efficacy in specialized tasks such as spider classification (Z. K. Deng & Rodriguez, 2024), indicating its potential for varied applications. Swin, leveraging a modern transformer architecture, provides an opportunity to compare CNNs with transformer-based models, which are increasingly relevant in computer vision research. All three base models are moderately sized (ResNet50: 25.6M parameters, ConvNeXtV2 Tiny: 28.6M, Swin Tiny Patch4 Window7: 28.3M), ensuring that they remain manageable with limited computational resources. Another important reason for selecting these models was the availability of pretrained weights from the ImageNet-1K dataset (J. Deng et al., 2009). Throughout this paper, we will refer to these base models only by their shorter names ResNet, ConvNeXtV2, and Swin.

A total of 313 spider-related images, resized to 224×224 pixels, were used as input. Corresponding labels, consisting of fear ratings, were obtained from our dataset. To enhance robustness and generalizability, we applied standard image augmentations (Shorten & Khoshgoftaar, 2019) on the training datasets, including random horizontal flips, small rotations, translations, shearing, scaling, color jittering, filling, and Gaussian blurring.

To obtain task-adapted models for regression, we replaced each base model’s original classification layer with a specialized output head: three hidden layers with 256 units each, with dropout and a linear layer first, followed by rectified linear unit (ReLU) activations, batch normalization, dropout, and linear transformations. A final linear unit produced a single continuous output. We did not constrain or clip this output during the forward pass. After inference, predictions were post-hoc clipped to the 0–100 range to

match the rating scale. We refer to the resulting network as the *task-adapted model* (e.g., the ResNet-based task-adapted model). We reserve *architecture* for design families (e.g., CNN vs transformer).

Our training involved two stages—partial and full fine-tuning. In partial fine-tuning, pretrained layers (from ImageNet-1K) were frozen and only the new head was trained. In full fine-tuning, all layers were updated. Each base model was evaluated under two configurations: partial and full fine-tuning. This yielded six model configurations in total. We refer to each combination of base model (ResNet, ConvNeXtV2, or Swin) and fine-tuning stage (partial or full fine-tuning) as a model configuration; each configuration was trained multiple times within cross-validation, producing multiple trained instances.

All three base models were sourced from the timm Python library (Wightman, 2019) with pretrained weights and implemented in PyTorch (Paszke et al., 2019). Training was conducted on an NVIDIA RTX 4080 GPU with 16 GB VRAM.

Model Evaluation

Dual-Level Data Partitioning (Participants and Images)

To prevent overlap at both the participant and image levels, we applied a two-step partitioning scheme. First, we averaged fear ratings for each image separately within two non-overlapping participant groups (A and B). Second, during the 5-fold cross-validation procedure described in the next subsection, images assigned to the training folds were represented only by the group-A means, whereas images in the held-out test fold were represented only by the group-B means. Consequently, no participant and no image contributed to both training and test data within a fold iteration, preventing overlap and eliminating data leakage.

We randomly split the 148 participants once into two disjoint groups (A and B) using a fixed random seed and kept this split fixed across all analyses. For each image we computed two targets: group-A mean and group-B mean. In every fold and repetition, models were trained/validated on group-A means for training images and evaluated on

group-B means for held-out images. The group size was 74 in both groups. Distributions of group-A and group-B image means are shown in Appendix Figures A2 and A3.

Cross-Validation and Hyperparameter Search

The study implemented a multi-stage nested cross-validation (CV) and hyperparameter search procedure to optimize and evaluate the performance of the models (Hastie et al., 2001). This process included three main loops. The first loop performed five repetitions of random splits, each creating 5-folds, to ensure robust results. The second loop, the outer CV, then used these same splits, using optimal hyperparameters derived from the inner CV. The third loop (inner CV) was used for hyperparameter tuning via random search. It consisted of another 5-fold CV. In each outer repetition, the 5-fold outer CV produced five task-adapted model instances per model configuration, each trained on four folds and evaluated on its own held-out test fold. Across the five repetitions, this yielded 25 trained instances per configuration. Each image received exactly one held-out prediction per repetition (five in total).

The batch size was fixed at 16 and the AdamW optimizer (Kingma & Ba, 2017; Loshchilov & Hutter, 2019) was used. Mean squared error (MSE) was used as both the loss function during training and as the metric for evaluating model performance at each epoch. To avoid gradient saturation and bias from bounded output constraints (e.g., hard clipping/sigmoid/tanh), we left the final unit unconstrained and computed MSE on raw predictions; clipping to 0–100 was applied only post hoc, and we stored both raw and clipped predictions. At the end of each epoch, evaluation was conducted on an internal validation set, which consisted of 20% of the training data (group-A means). The checkpoint (a snapshot of the model’s weights) corresponding to the lowest MSE on this validation set was selected as the best-performing model instance. No early stopping and no learning rate schedulers were used.

As mentioned above, the models were trained in two stages. In the initial partial fine-tuning stage, only the new final layers were trained using hyperparameters selected

from these ranges: a learning rate from $1e-3$ to $1e-1$ (on a logarithmic scale), weight decay from $1e-6$ to $1e-3$ (on a logarithmic scale), dropout rate from 0.2 to 0.5, and a number of epochs from 10 to 50. In the subsequent full fine-tuning stage—where all layers were updated—the hyperparameter search was conducted over the following ranges: a learning rate from $1e-6$ to $1e-4$ (on a logarithmic scale), weight decay from $1e-6$ to $1e-3$ (on a logarithmic scale), and 10 to 50 epochs.

The hyperparameter for the number of epochs was treated as an upper limit, as the best-validation checkpoint is often reached before this maximum. We defined the effective number of training epochs as the epoch at which the best-validation checkpoint was saved, plus a fixed buffer of 5 epochs. We then used this adjusted value for subsequent training and reporting. Thirty search trials (i.e., hyperparameter combinations) were conducted, and the hyperparameter set yielding the lowest loss was selected.

Within each outer repetition, each image appears exactly once in a held-out test fold, yielding one test-set (held-out) prediction per image per repetition; these predictions were stored for metric computation and ensembling.

Computation of Final Performance Metrics

With the optimal hyperparameters determined, in each outer repetition and fold iteration we trained a new model instance on the four training folds (group-A means) and evaluated it on the corresponding held-out test fold (group-B means). Only predictions from held-out test folds were used. We stored both raw and clipped predictions, but all reported metrics and analyses use the clipped (0—100) predictions.

Single-Model (Non-Ensembled) Performance. For each model configuration and each outer repetition, we concatenated the test-set predictions from its five folds and computed MAE, RMSE, and R^2 once on this concatenated test set. We then averaged these repetition-level metrics across the five outer repetitions to obtain the final single-model estimates reported in Table 1 (columns R^2 , MAE, RMSE). These estimates reflect the expected performance of a single trained model instance.

Ensembling Across Outer Repetitions. Separately, for each image we collected its five test-set predictions per model configuration (one from each outer repetition) and averaged them to obtain a per-image ensemble prediction. We then computed MAE, RMSE, and R^2 from these ensemble predictions against the corresponding group-B means. These ensemble metrics (R_{ens}^2 , MAE_{ens} , $RMSE_{ens}$ in Table 1) quantify the performance gain from averaging predictions of independently trained instances. No in-sample predictions were used.

Upper Bound Estimation of R^2 Using Intraclass Correlation Coefficient

To estimate the upper bound of the models’ predictive performance, we employed the Intraclass Correlation Coefficient (ICC). The ICC quantifies the proportion of variance due to true between-image differences and thus provides an upper bound on attainable R^2 for predicting image-level mean ratings. We used the ICC(2,k) variant from the R package psych (Revelle, 2024), which is suitable for two-way random effects and average measures, accommodating missing values in the dataset. To ensure a reliable estimate of the ICC, we used a bootstrapping approach to generate a distribution of values for various subsample sizes. We randomly sampled participant ratings (without replacement) from our full dataset, repeating the process 100 times for subsample sizes of 10, 20, 30, 40, 50, 60, 70, and 80. This method allowed us to examine how the ICC stabilizes as the number of raters increases, providing a reliable upper-bound estimate of the model’s performance based on empirical human agreement.

Learning Curve Analysis

A learning curve analysis was performed to demonstrate the effect of varying numbers of images on training performance, measured by MAE, RMSE and R^2 . Specifically, the analysis consisted of seven different dataset sizes: 50, 75, 100, 150, 200, 250 and 313 (complete dataset) images. The training procedure for the complete dataset was already part of our primary analysis and was therefore not repeated. For the other six sizes, training was performed as described for the full dataset, but with one additional measure:

to account for subsampling variability in each of the five outer repetitions, we created not only a different random CV split, but also a different random subsample. Using the same subsample in each iteration could lead to a biased estimate if it consists of images that are particularly difficult or easy for the model to predict. The results of these five iterations were then averaged to obtain the final MAE, RMSE and R^2 values for each dataset size. To visualize the trend, we fitted a three-parameter curve to the averaged scores of each size. For MAE and RMSE, we used exponential decay: $y(n) = a \cdot \exp(-b \cdot n) + c$. For R^2 , we used an exponential rise to a limit: $y(n) = a \cdot (1 - \exp(-b \cdot n)) + c$. The parameters (a, b, c) were estimated using nonlinear least squares in Python (`scipy.optimize.curve_fit`).

Explanations

To ensure the transparency and interpretability of the model’s predictions, we employed two explainable AI (XAI; Barredo Arrieta et al., 2020) approaches: attributions and feature visualization (FV). These methods provide insights into which aspects of the input data are most influential in the prediction process and how the internal components of the model behave during inference.

Attributions

To understand which regions of the input images were most important for the predictions, we used Grad-CAM (Selvaraju et al., 2020). This technique was developed for CNNs and generates a heatmap highlighting the areas in the images that significantly impact the model’s output. Because standard Grad-CAM relies on spatial convolutional feature maps, we restricted this analysis to the two CNN-based models (ResNet, ConvNeXtV2); transformer-specific alternatives for Swin produce token-level attributions that are not directly comparable to our pixel-level spider masks.

We used the Python package Captum (Kokhlikyan et al., 2020) to generate the Grad-CAM heatmaps. Grad-CAM calculates gradients of the target prediction with respect to the activation maps of a specified layer, in this case, the final convolutional layer. These gradients reveal the influence of each feature map on the final decision. Grad-CAM

combines the feature maps using the gradients as weights to produce a heatmap that highlights the regions of the input image most relevant to the model’s prediction.

To further validate the heatmaps generated by Grad-CAM, we obtained additional annotations using Label Studio (labelstud.io). A trained researcher from our laboratory used Label Studio’s *Semantic Segmentation with Masks* annotation method to precisely delineate the pixels corresponding to the spiders’ positions in each image. We focused only on the images that actually contained spiders, resulting in a total of 282 images being analyzed. This manual annotation facilitated an accurate comparison between the generated heatmaps and the actual locations of the spiders.

In this analysis, we selected the model configuration with the lowest MAE from each of the two CNN base models—whether it was achieved through partial or full fine-tuning—based on our primary analysis. Previously, we performed five cross-validated training runs for each model configuration, producing five final model checkpoints. For each checkpoint, we generated heatmaps for all images. We then averaged these five sets of heatmaps to create a composite representation, resulting in one final heatmap per image and model configuration.

To evaluate how well Grad-CAM attributions correspond to the spider locations, we analyzed mean Grad-CAM activation levels. We calculated the mean activations both inside the spider-masked area and outside the mask for each of the 282 images. Raw Grad-CAM scores were used without any per-image rescaling. A one-sided paired t -test on the 282 paired differences was used to determine if the mean activation within the mask was significantly greater than the mean activation outside the mask. Finally, we computed Cohen’s d for paired samples to quantify the magnitude of this effect. Although mask size varied widely across images (from approximately 5–80% of pixels), all images were given equal weight in the analysis.

Feature Visualization

We performed FV (Olah et al., 2017) using torch-lucent (Kiat, 2020) to synthesize input images that maximize the final scalar output (fear) of the task-adapted ResNet model trained on the full dataset with the best-performing training strategy (lowest MAE). We restricted FV to ResNet because, under identical priors and optimization settings, ConvNeXtV2 yielded high-frequency, iridescent patterns with low human interpretability. Adapting FV to ConvNeXtV2 would require alternative, stronger generative priors and is beyond scope. Transformer models (Swin) were not included due to non-comparable token-level feature spaces. We generated 500 synthetic images per base model. Representative ResNet FVs are shown in Results (Figure 4); the full set and quantitative summaries are provided in Appendix E.

Image-Category-Based Error Analysis

For this analysis, we used the image categories defined by Karner, Obenaus, et al. (2024), where each image had been annotated along 12 criteria: *spider in picture*, *cobweb in picture*, *number of spiders*, *subjective distance*, *environment*, *texture*, *eyes*, *eating prey*, *subjective size*, *perspective*, *color of picture*, and *prominent legs*. The category definitions and level counts (including “not evaluable” where applicable) are provided in the Appendix F.

For each base model, we analyzed the best-performing configuration (lowest MAE from the primary analysis). Per image, we computed absolute error as the mean across the five outer repetitions. For each criterion, we summarized categories by sample size and proportion, mean/median and IQR of absolute error, contribution to total absolute error (share), and over/under-representation relative to frequency ($\Delta = \text{share} - \text{frequency}$). Within each criterion, we tested category differences using the Kruskal–Wallis test and controlled the false discovery rate across criteria within each model using Benjamini–Hochberg; we report epsilon-squared (ϵ^2) as an effect size. Stratified bootstrap 95% confidence intervals were computed for per-category means and shares. Categories

with small sample sizes ($n < 10$) were summarized descriptively without inferential claims.

Results

Predictive Performance

As shown in Table 1, the task-adapted models explained a substantial portion of the variance in human fear ratings, with R^2 values ranging from 0.503 to 0.584. The mean absolute error (MAE) values for the individual models were between 10.104 and 11.025, while the root mean squared error (RMSE) values ranged from 12.871 to 14.067. Among the three base models, Swin and ConvNeXtV2 consistently outperformed ResNet, with the highest individual R^2 of 0.584 belonging to the fully fine-tuned Swin-based model. We estimated the upper bound for the model’s performance using the ICC(2,k) analysis, conducted on a subsample of 80 participants. This analysis revealed a mean inter-rater reliability of 0.971 with a standard deviation of 0.003 (see Table B1 in Appendix B). As shown in Figure B1, the ICC values stabilized at a high level as the number of raters increased, indicating that a perfect predictive model could at best achieve an R^2 of 0.971. Ensembling the models consistently enhanced performance across all base-model configurations. For instance, the ensemble of fully fine-tuned Swin-based models achieved the highest R^2 of 0.621, an absolute increase of 0.037 R^2 points over the best single model (0.584), corresponding to a 6.3% relative improvement. This ensemble approach also reduced the MAE to 9.670 and the RMSE to 12.283, showing a decrease in prediction error compared to the individual models. Figure 1 illustrates the predictions for the best-performing configuration for each base model.

Table 1*Predictive performance of ResNet-, ConvNeXtV2-, and Swin-based models*

Model	Fine-tuning	R^2	MAE	RMSE	R^2_{ens}	MAE_{ens}	$RMSE_{ens}$
ResNet	Partial	0.503	11.025	14.067	0.557	10.511	13.287
ResNet	Full	0.525	10.709	13.756	0.575	10.198	13.019
ConvNeXtV2	Partial	0.563	10.426	13.191	0.608	10.017	12.491
ConvNeXtV2	Full	0.573	10.368	13.044	0.617	9.924	12.350
Swin	Partial	0.565	10.327	13.163	0.605	9.928	12.552
Swin	Full	0.584	10.104	12.871	0.621	9.670	12.283

Note. R^2 = coefficient of determination; MAE = mean absolute error; RMSE = root mean squared error; ens = ensemble across outer repetitions.

Learning Curve Analysis

The learning curve analysis focused on varying the dataset by the number of images and observing the effect on model performance, i.e. how well the models generalize to unseen images. For our analysis, we used all three base model under partial fine-tuning. Figure 2 illustrates model performance across varying dataset sizes (50, 75, 100, 150, 200, 250, and 313 images). Each curve was fitted to the actual data points, represented by cross-shaped markers, illustrating the enhancement of model performance against held-out test sets as the number of available images increases. The results showed that the R^2 values for all three models increased monotonically up to the maximum dataset size of 313 images. At this point, a plateau was reached, suggesting that more data, i.e. more images, would not lead to much better performance from this point on. Furthermore, model performance significantly declined when the dataset size fell below 100 images, as evidenced by R^2 values dropping below 0.4. Numeric values of all empirical data points are reported in Table C1, and the three fitted parameters (a, b, c) for every model-metric pair are summarized in Table C2.

Figure 1

Observed fear versus ensemble predictions with the identity (perfect-prediction) line

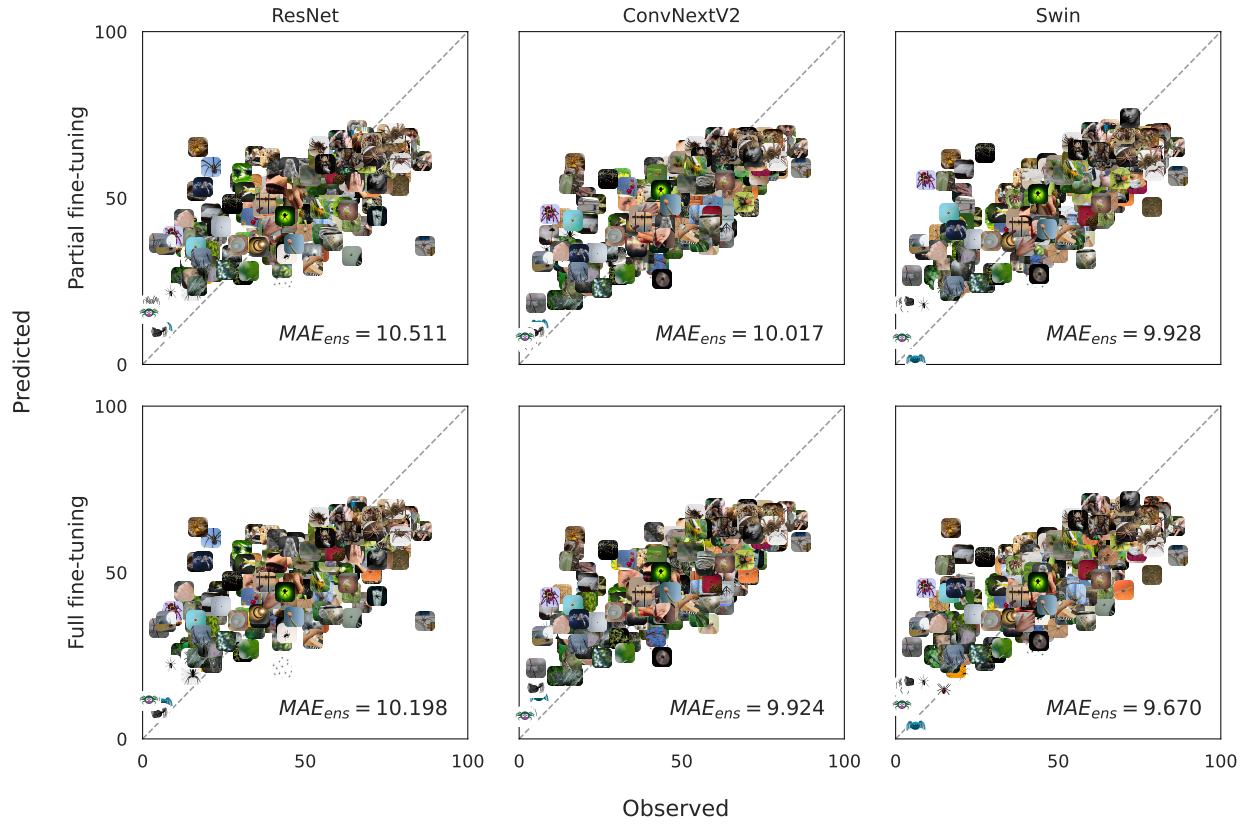
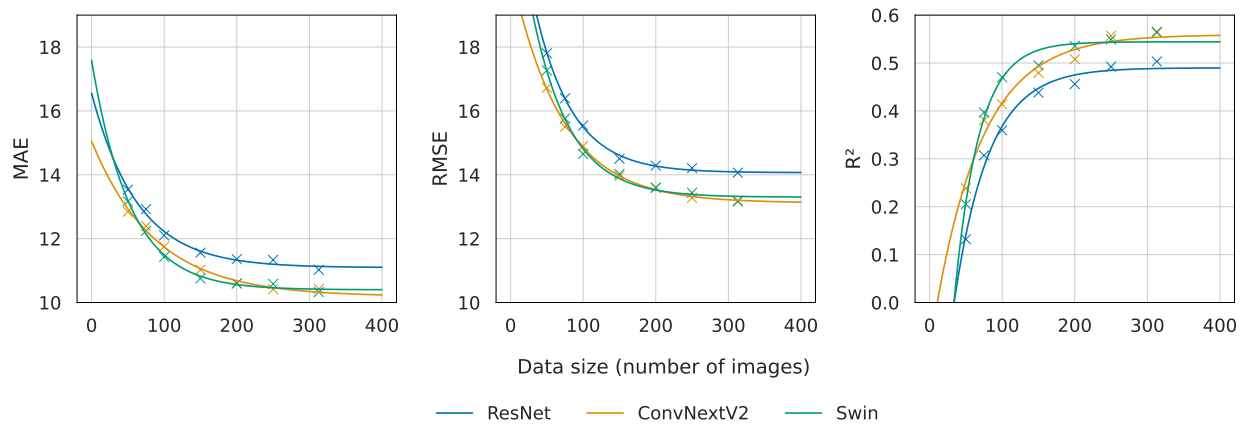


Figure 2

Learning Curves for Mean Absolute Error (MAE), Root Mean Squared Error (RMSE), and Variance Explained (R^2)



Model Explanations

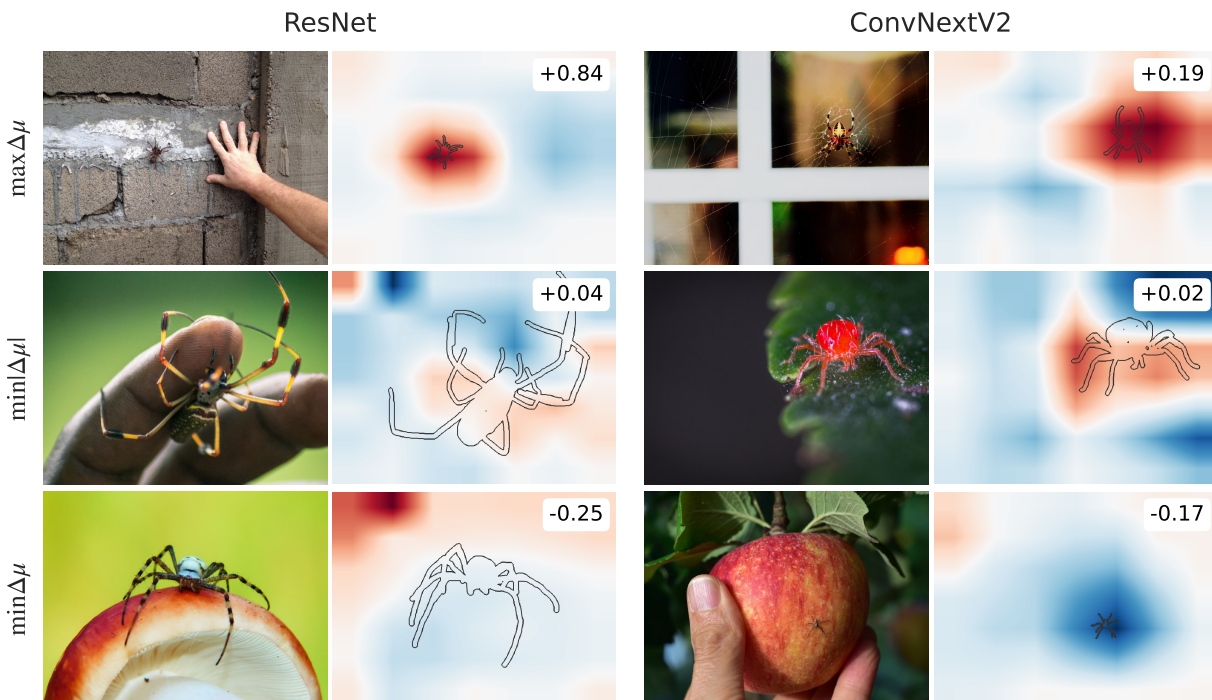
Figure 3 shows a selection from the resulting Grad-CAM heatmaps, illustrating patterns and foci related to each model’s predictions. The figure presents three representative examples for each task-adapted model, ordered to show the model’s focus from areas outside spiders to areas occupied by spiders. The first example, with the maximum activation difference, illustrates higher activation inside the spider mask. The second example, with an activation difference closest to zero, represents a balanced focus where activations were roughly the same inside and outside the mask. The third example, with the minimum activation difference (which may be negative), shows higher activation outside the spider mask. The full set of these heatmaps is available at the provided OSF repository.

The analysis revealed the extent to which the convolutional neural network (CNN) models focused on spider areas during fear prediction. For both ResNet- and ConvNeXtV2-based task-adapted models, activations within the spider mask were significantly higher than outside the mask in 282 images featuring spiders, with ResNet showing a Cohen’s d of 0.43 and ConvNeXtV2 a Cohen’s d of 0.38 (both $p < 0.001$) (see Appendix D). These results suggest that the two CNN-based models similarly emphasize spider locations in fear prediction. Most importantly, the results show a considerable overlap between the heatmap regions and the actual spider locations, confirming the model’s ability to focus on features relevant to human fear judgments.

Supplementary feature visualizations for the ResNet-based model show coherent spider-like structure (Figure 4); 83.8% (95% CI 80.3–86.8%) were classified as *spider* (top-1) by an unadapted ResNet-ImageNet classifier ($N = 500$); summary statistics are provided in Table E1. In contrast, ConvNeXtV2 FV attempts were not human-interpretable and reached 13.0% (95% CI 10.3–16.2%) top-1 *spider* ($N = 500$).

Figure 3

Example Grad-CAM Heatmaps Highlighting Model Focus During Fear Predictions



Note. Values in the heatmaps show the difference in raw Grad-CAM activation scores between in-mask and out-mask areas: $\Delta\mu = \mu_{in} - \mu_{out}$. Positive $\Delta\mu$ indicates higher activation inside the mask (top row), while negative $\Delta\mu$ indicates higher activation outside the mask (bottom row). The image in the middle row has a $\Delta\mu$ value closest to zero, indicating similar activation inside and outside the mask. Examples were restricted to images with observed fear ≥ 40 (image-level mean across held-out raters); this criterion was used only for visualization and did not affect quantitative analyses.

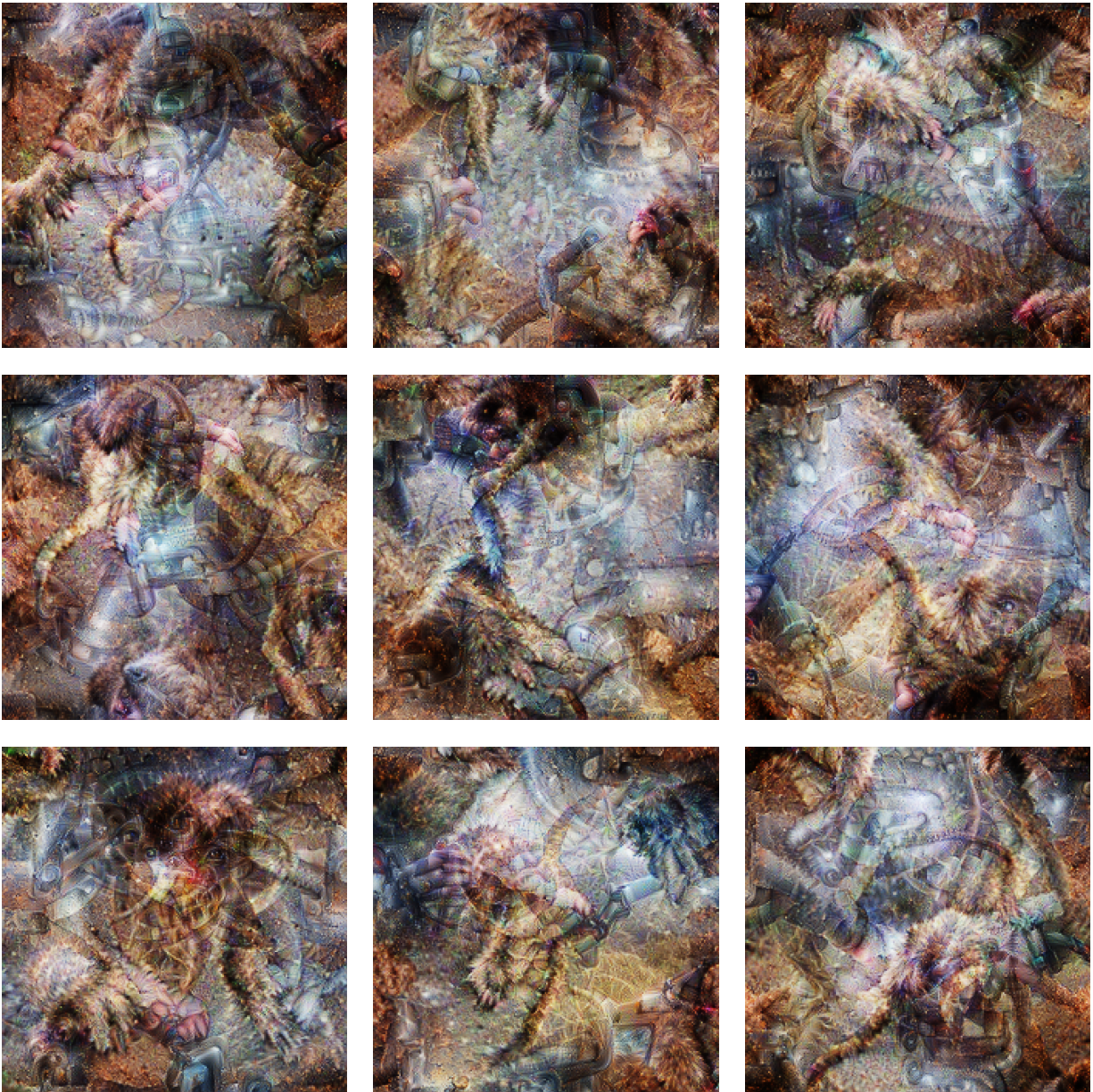
Error Analysis

Figure 5 shows, for each base model, the top three criteria with category error shares versus frequencies; Table 2 reports omnibus tests and the hardest and easiest categories within those criteria.

Across models, distant (subjective distance), and artificial, painted or comic spider (spider in picture) were consistently over-represented in MAE ($\Delta \approx +4.0 - +7.2$ percentage points), whereas close (subjective distance), hairy (texture), and spider (spider in picture) tended to be under-represented. Environment ranked among the top three criteria only for

Figure 4

ResNet Feature Visualizations for the Final Output Node



Note. The figure shows nine synthetic example images that maximally activate the task-adapted model's fear rating predictions, revealing the learned features that the model associates with high fear.

Swin; within this criterion, civilization scenes were more error-prone than nature scenes.

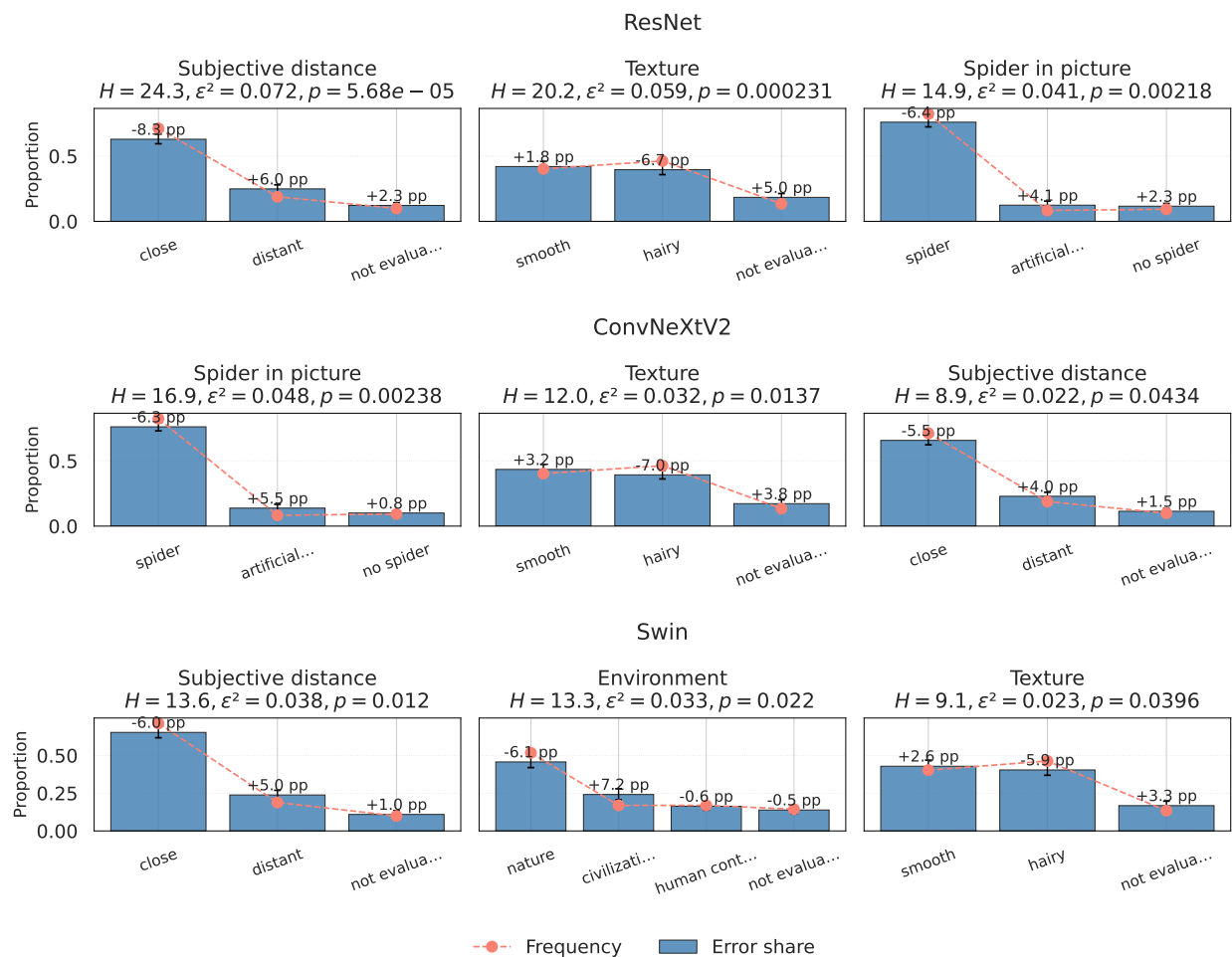
Each model showed a distinct pattern in its category-wise errors. The ResNet-based model displayed the most varied error profile, with significant differences found in 10 of the 12 criteria (Kruskal–Wallis, FDR). Its top three error drivers were subjective distance, texture, and whether a spider was present in the image. The most difficult categories were distant spiders ($\Delta + 6.0$ pp) and artificial or comic spiders ($\Delta + 4.1$ pp), with effect sizes ranging from small to moderate. In comparison, ConvNeXtV2 and Swin had more focused error profiles. ConvNeXtV2’s errors were significantly affected by just three criteria: spider in picture, subjective distance, and texture. Its biggest challenges were with artificial spiders ($\Delta + 5.5$ pp), not evaluable images ($\Delta + 3.8$ pp), and distant spiders ($\Delta + 4.0$ pp). Similarly, Swin showed significant error differences in four criteria, with the most important being subjective distance, environment, and texture. It struggled the most with images of spiders in civilization ($\Delta + 7.2$ pp), followed by distant spiders ($\Delta + 5.0$ pp). Both models had small effect sizes for these criteria. Full per-category statistics are provided in Appendix F.

Discussion

This study shows that pretrained vision models adapted for regression can predict human fear ratings for spider-related images with moderate accuracy. Across model configurations, explained variance reached up to $R^2 = 0.584$ for single models and $R^2 = 0.621$ when ensembling across outer repetitions, with correspondingly low MAE and RMSE. Learning curves rose monotonically and approached a plateau at the full dataset size (313 images), while performance deteriorated below approximately 100 images. Explainability analyses showed that convolutional neural networks (CNNs) concentrated on spider regions (Grad-CAM) and learned spider-like features (feature visualization; FV), supporting clinical interpretability. Category-wise errors concentrated in distant viewpoints, artificial/painted depictions, and civilization environments, whereas images with close viewpoints, hairy textures, and real spiders showed lower error.

Figure 5

Error Share Versus Category Frequency by the Top Three Criteria Across Base Models



Note. Composite figure with panels per base model; within each, the top three criteria (by Kruskal–Wallis effect size with FDR) are shown. Blue bars indicate each category’s share of total absolute error (summing to 1 within a criterion); black caps are 95% stratified bootstrap CIs. The dashed line shows category frequency (proportion of images). Bar higher than the dashed line indicates over-representation in error ($\Delta > 0$); lower indicates under-representation ($\Delta < 0$). Errors are the mean absolute error averaged across five outer repetitions for the best-performing configuration per base model. Small- n categories may have wide CIs; “not evaluable” levels are included where present. Full statistics are reported in Appendix F.

Table 2

Error Analysis Summary by Model and Criterion

Model	Criterion	Omnibus			Hardest Category				Easiest Category		
		H	ε^2	FDR p	Name	Mean AE	n	Share (%)	Delta (pp)	Name	Mean AE
ConvNeXtV2	spider in picture	16.88	0.048	0.002	artificial, pai...	17.24	26	13.8	5.5	spider	9.58
ConvNeXtV2	subjective distance	8.87	0.022	0.043	distant	12.59	59	22.9	4.0	close	9.57
ConvNeXtV2	texture	11.99	0.032	0.014	not evaluable	13.30	42	17.2	3.8	hairy	8.80
ResNet	spider in picture	14.86	0.041	0.002	artificial, pai...	15.97	26	12.4	4.1	spider	9.87
ResNet	subjective distance	24.35	0.072	< .001	distant	14.13	59	24.9	6.0	close	9.46
ResNet	texture	20.16	0.059	< .001	not evaluable	14.69	42	18.4	5.0	hairy	9.15
Swin	environment	13.32	0.033	0.022	civilization	14.40	53	24.1	7.2	nature	8.92
Swin	subjective distance	13.64	0.038	0.012	distant	12.77	59	23.8	5.0	close	9.26
Swin	texture	9.06	0.023	0.040	not evaluable	12.61	42	16.7	3.3	hairy	8.81

Note. Omnibus = Kruskal–Wallis across categories within criterion; ε^2 = epsilon-squared effect size. FDR p = Benjamini–Hochberg adjusted p-value across criteria. Share (%) = category’s contribution to total absolute error within criterion; Delta (pp) = over/under-representation relative to category frequency. AE = mean absolute error averaged across five outer repetitions.

Predictive Performance and Clinical Relevance

Transfer learning from ImageNet-1K enabled all three base models to capture variance in fear ratings, with Swin and ConvNeXtV2 outperforming ResNet, consistent with recent advances in both convolutional and transformer-based architectures (Yosinski et al., 2014; Liu et al., 2021; Woo et al., 2023). The ensemble of multiple model instances further improved accuracy, aligning with established benefits of model aggregation, and is directly useful when stable predictions are needed in clinical pipelines. In applied settings such as exposure therapy, the obtained performance levels can already support adaptive selection and sequencing of stimuli, with transparency aided by the explainable AI analyses (XAI; Barredo Arrieta et al., 2020; van der Velden et al., 2022).

Data Requirements and Learning Curves

Learning curves indicated that model performance increases steadily with more images but begins to plateau at the current dataset size, suggesting diminishing returns without added diversity. The sharp decline below ~100 images highlights the importance of maintaining sufficient sample sizes for reliable generalization. Together with the ICC upper bound, these results suggest two complementary paths: increasing dataset size and diversity (e.g., contexts, viewpoints) and improving model efficiency to better leverage available data.

Model Explanations and Interpretability

Grad-CAM analyses for the two CNNs showed significantly higher activations within spider masks than outside, with small-to-moderate effect sizes, indicating that predictions are predominantly driven by phobia-relevant regions (Selvaraju et al., 2020). FV (Appendix E) revealed spider-like textures and shapes (e.g., legs, body/eyes, earthy tones), offering a global view of features associated with high predicted fear (Olah et al., 2017). Together, attributions and FV support that the models rely on meaningful cues—an important prerequisite for clinical trust and deployment.

Category-Wise Error Patterns

Analysis of errors by category showed that absolute errors were concentrated in distant viewpoints, artificial/painted depictions, and civilization contexts, while close viewpoints, hairy textures, and real spiders had lower error rates. These patterns were consistent across the best-performing models, suggesting the errors are due to data conditions—such as reduced visibility of informative cues, background clutter, and domain shift—rather than specific architectural weaknesses. To improve performance, future dataset curation and augmentation should increase the representation of these difficult conditions. Training could also prioritize them using methods like category-weighted sampling (to give these examples more influence) and curriculum learning (to progressively introduce harder examples). Furthermore, reporting per-category performance and model uncertainty could support clinical oversight. Future research should jointly model these criteria to understand their interactions and explore domain adaptation techniques to reduce errors in challenging contexts.

Architectural Considerations

Swin and ConvNeXtV2 consistently outperformed ResNet at comparable parameter scales, suggesting benefits from updated architectural designs and inductive biases. While transformers are increasingly competitive in vision tasks, CNNs remained attractive here due to their compatibility with established attribution tools and strong performance. These complementary strengths argue for exploring hybrid and ensemble strategies tailored to clinical constraints. As a limitation, our XAI analyses focused on CNNs; Grad-CAM was applied to ResNet and ConvNeXtV2. FV was restricted to ResNet because ConvNeXtV2 produced non-interpretable, high-frequency patterns under standard Lucent priors; adapting FV for ConvNeXtV2 would require stronger generative priors (e.g., diffusion-guided) and is beyond scope. Transformer-appropriate XAI for Swin is deferred to future work.

Implications and Outlook

The demonstrated accuracy and interpretability position these models as building blocks for adaptive computerized exposure therapy (Choy et al., 2007; Craske et al., 2014). A key limitation, however, is that our models estimate average group-level fear ratings, whereas clinical application requires accurate per-person predictions. The error for individual ratings would be higher than for our current group-level estimations. Future work should therefore (a) focus on personalization by incorporating participant-level predictors to tailor computerized exposure therapy to individual needs, (b) expand and diversify image corpora to push beyond the current learning-curve plateau, and (c) refine model training (e.g., stronger fine-tuning protocols and ensembling). In parallel, integrating these predictors into real-time pipelines can enable on-the-fly stimulus selection and progression tracking, with XAI outputs supporting clinician oversight. Ultimately, scaling data and leveraging modern architectures is expected to yield reliable, transparent fear estimation that supports more personalized, efficient, and accessible interventions.

Data Availability Statement

The data used in this study are available from several previously published papers. The spider images are from Zhang et al. (2025), the fear ratings for these images are from Karner, Zhang, et al. (2024), and the categorization taxonomy for the images is from Karner, Obenaus, et al. (2024). The code and materials to reproduce the analysis are available at <https://osf.io/8b5a2/>.

CRedit Authorship Contribution Statement

DP: Conceptualization, Investigation, Methodology, Software, Formal Analysis, Data Curation, Visualization, Writing - Original Draft, Writing - Review & Editing. DS: Methodology, Writing - Review & Editing. MZ: Data Curation, Writing - Review & Editing. AK: Data Curation, Writing - Review & Editing. JA: Formal Analysis, Writing - Review & Editing. FS: Resources, Supervision, Writing - Review & Editing. FM: Supervision, Conceptualization, Methodology, Writing - Original Draft, Writing - Review

& Editing.

Acknowledgments

We would like to thank Jázmin Mikó for significant contributions to the spider labeling, which were instrumental in advancing this project.

Competing Interests

The authors declare no competing interests.

References

- Barredo Arrieta, A., Díaz-Rodríguez, N., Del Ser, J., Bennetot, A., Tabik, S., Barbado, A., Garcia, S., Gil-Lopez, S., Molina, D., Benjamins, R., Chatila, R., & Herrera, F. (2020). Explainable Artificial Intelligence (XAI): Concepts, taxonomies, opportunities and challenges toward responsible AI. *Information Fusion*, 58, 82–115. <https://doi.org/10.1016/j.inffus.2019.12.012>
- Choy, Y., Fyer, A. J., & Lipsitz, J. D. (2007). Treatment of specific phobia in adults. *Clinical Psychology Review*, 27(3), 266–286. <https://doi.org/10.1016/j.cpr.2006.10.002>
- Craske, M. G., Treanor, M., Conway, C. C., Zbozinek, T., & Vervliet, B. (2014). Maximizing exposure therapy: An inhibitory learning approach. *Behaviour Research and Therapy*, 58, 10–23. <https://doi.org/10.1016/j.brat.2014.04.006>
- Davey, G. C. L. (2007). Psychopathology and treatment of specific phobias. *Psychiatry*, 6(6), 247–253. <https://doi.org/10.1016/j.mppsy.2007.03.007>
- Deng, J., Dong, W., Socher, R., Li, L.-J., Kai Li, & Li Fei-Fei. (2009). ImageNet: A large-scale hierarchical image database. *2009 IEEE Conference on Computer Vision and Pattern Recognition*, 248–255. <https://doi.org/10.1109/CVPR.2009.5206848>
- Deng, Z. K., & Rodriguez, J. J. (2024). Look out for dangerous spiders: Araneae classification using deep learning methods. *2024 IEEE Southwest Symposium on Image Analysis and Interpretation (SSIAI)*, 134–137. <https://doi.org/10.1109/SSIAI59505.2024.10508676>

- Hastie, T., Tibshirani, R., & Friedman, J. (2001). *The elements of statistical learning*. Springer New York Inc.
- He, K., Zhang, X., Ren, S., & Sun, J. (2015). Deep residual learning for image recognition. *Proceedings of the IEEE Conference on Computer Vision and Pattern Recognition*, 770–778. <https://doi.org/10.48550/arXiv.1512.03385>
- Healey, A., Mansell, W., & Tai, S. (2017). An experimental test of the role of control in spider fear. *Journal of Anxiety Disorders*, 49, 12–20. <https://doi.org/10.1016/j.janxdis.2017.03.005>
- Karner, A., Obenaus, L., Zhang, M., Lor, C., Kostorz, K., Pegler, D., Leopold, M.-L., Melinscak, F., Steyrl, D., & Scharnowski, F. (2024, June 14). *Visual attributes of spiders associated with aversiveness in spider-fearful individuals: A machine learning analysis*. <https://doi.org/10.31234/osf.io/ht2pr>
- Karner, A., Zhang, M., Lor, C. S., Steyrl, D., Götzendorfer, S. J., Weidt, S., Melinscak, F., & Scharnowski, F. (2024). The “SpiDa” dataset: Self-report questionnaires and ratings of spider images from spider-fearful individuals. *Frontiers in Psychology*, 15. <https://doi.org/10.3389/fpsyg.2024.1327367>
- Kiat, L. S. (2020). *Torch-lucent* (Version 0.1.8). <https://github.com/greentfrapp/lucent>
- Kim, H.-R., Kim, Y.-S., Kim, S. J., & Lee, I.-K. (2018). Building emotional machines: Recognizing image emotions through deep neural networks. *IEEE Transactions on Multimedia*, 20(11), 2980–2992. <https://doi.org/10.1109/TMM.2018.2827782>
- Kingma, D. P., & Ba, J. (2017, January 29). *Adam: A method for stochastic optimization*. arXiv: 1412.6980 [cs]. Retrieved April 1, 2023, from <http://arxiv.org/abs/1412.6980>
- Kokhlikyan, N., Miglani, V., Martin, M., Wang, E., Alsallakh, B., Reynolds, J., Melnikov, A., Kliushkina, N., Araya, C., Yan, S., & Reblitz-Richardson, O. (2020, September 16). *Captum: A unified and generic model interpretability library for PyTorch*. arXiv: 2009.07896 [cs]. <https://doi.org/10.48550/arXiv.2009.07896>

- LeCun, Y., Bengio, Y., & Hinton, G. (2015). Deep learning. *Nature*, *521*(7553), 436–444.
<https://doi.org/10.1038/nature14539>
- Leys, C., Ley, C., Klein, O., Bernard, P., & Licata, L. (2013). Detecting outliers: Do not use standard deviation around the mean, use absolute deviation around the median. *Journal of Experimental Social Psychology*, *49*(4), 764–766.
<https://doi.org/10.1016/j.jesp.2013.03.013>
- Liu, Z., Lin, Y., Cao, Y., Hu, H., Wei, Y., Zhang, Z., Lin, S., & Guo, B. (2021, August 17). *Swin transformer: Hierarchical vision transformer using shifted windows*. arXiv: 2103.14030 [cs]. <https://doi.org/10.48550/arXiv.2103.14030>
- Loshchilov, I., & Hutter, F. (2019, January 4). *Decoupled weight decay regularization*. arXiv: 1711.05101 [cs]. <https://doi.org/10.48550/arXiv.1711.05101>
- Olah, C., Mordvintsev, A., & Schubert, L. (2017). Feature Visualization. *Distill*, *2*(11), e7.
<https://doi.org/10.23915/distill.00007>
- Paszke, A., Gross, S., Massa, F., Lerer, A., Bradbury, J., Chanan, G., Killeen, T., Lin, Z., Gimelshein, N., Antiga, L., Desmaison, A., Köpf, A., Yang, E., DeVito, Z., Raison, M., Tejani, A., Chilamkurthy, S., Steiner, B., Fang, L., . . . Chintala, S. (2019, December 3). *PyTorch: An Imperative Style, High-Performance Deep Learning Library*. arXiv: 1912.01703 [cs, stat]. Retrieved November 19, 2022, from <http://arxiv.org/abs/1912.01703>
- Revelle, W. (2024, December 23). *Psych: Procedures for psychological, psychometric, and personality research* (Version 2.4.12). Retrieved February 6, 2025, from <https://cran.r-project.org/web/packages/psych/index.html>
- Russell, S. J. (2020). *Human compatible: Artificial intelligence and the problem of control*. Penguin Books.
- Sanders, C. A., & Nosofsky, R. M. (2020). Training deep networks to construct a psychological feature space for a natural-object category domain. *Computational Brain & Behavior*, *3*(3), 229–251. <https://doi.org/10.1007/s42113-020-00073-z>

- Selvaraju, R. R., Cogswell, M., Das, A., Vedantam, R., Parikh, D., & Batra, D. (2020). Grad-CAM: Visual explanations from deep networks via gradient-based localization. *International Journal of Computer Vision*, *128*(2), 336–359.
<https://doi.org/10.1007/s11263-019-01228-7>
- Shorten, C., & Khoshgoftaar, T. M. (2019). A survey on image data augmentation for deep learning. *Journal of Big Data*, *6*(1), 60. <https://doi.org/10.1186/s40537-019-0197-0>
- Sun, M., Yang, J., Wang, K., & Shen, H. (2016). Discovering affective regions in deep convolutional neural networks for visual sentiment prediction. *2016 IEEE International Conference on Multimedia and Expo (ICME)*, 1–6.
<https://doi.org/10.1109/ICME.2016.7552961>
- van der Velden, B. H. M., Kuijf, H. J., Gilhuijs, K. G. A., & Viergever, M. A. (2022). Explainable artificial intelligence (XAI) in deep learning-based medical image analysis. *Medical Image Analysis*, *79*, 102470.
<https://doi.org/10.1016/j.media.2022.102470>
- Wightman, R. (2019). PyTorch image models. *GitHub*.
<https://doi.org/10.5281/zenodo.4414861>
- Woo, S., Debnath, S., Hu, R., Chen, X., Liu, Z., Kweon, I. S., & Xie, S. (2023, January 2). *ConvNeXt V2: Co-designing and scaling ConvNets with masked autoencoders*. arXiv: 2301.00808 [cs]. <https://doi.org/10.48550/arXiv.2301.00808>
- Yosinski, J., Clune, J., Bengio, Y., & Lipson, H. (2014). How transferable are features in deep neural networks? *Advances in Neural Information Processing Systems*, 3320–3328. <https://doi.org/10.48550/arXiv.1411.1792>
- You, Q., Luo, J., Jin, H., & Yang, J. (2015). Robust image sentiment analysis using progressively trained and domain transferred deep networks. *Proceedings of the AAAI Conference on Artificial Intelligence*, *29*(1).
<https://doi.org/10.1609/aaai.v29i1.9179>

Zhang, M., Karner, A., Kostorz, K., Shea, S., Steyrl, D., Melinscak, F., Sladky, R., Lor, C. S., & Scharnowski, F. (2025). SpiDa-MRI: Behavioral and (f)MRI data of adults with fear of spiders. *Scientific Data*, *12*(1), 284.
<https://doi.org/10.1038/s41597-025-04569-w>

Appendix A
Data Descriptives

Table A1

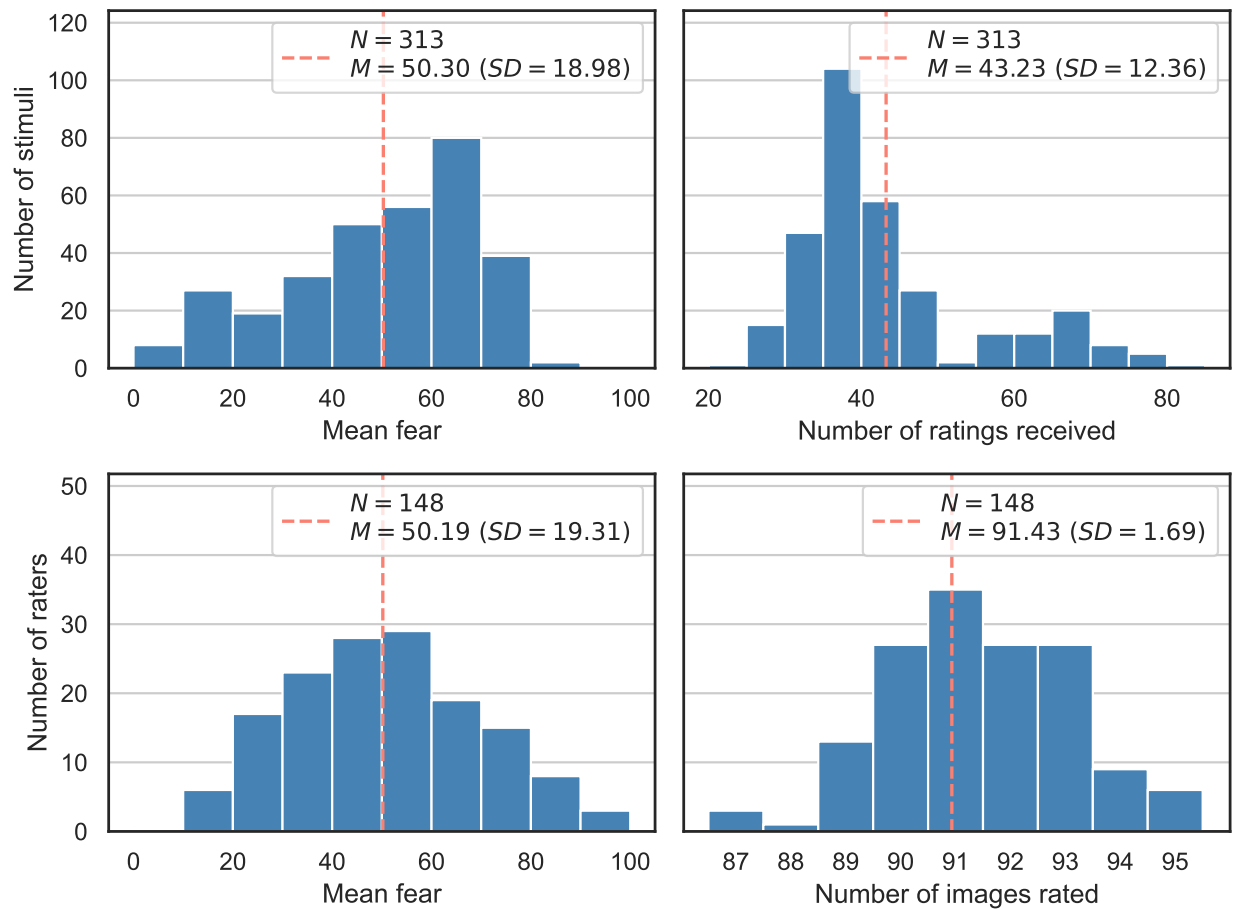
Frequency of Stimuli by Range of Mean Fear Ratings

Fear range	Number of stimuli	Percentage of stimuli (%)
0.00–20.00	35	11.2
20.00–40.00	51	16.3
40.00–60.00	106	33.9
60.00–80.00	119	38.0
80.00–100.00	2	0.6
Total (0–100)	313	100.0

Note. Fear scores are continuous from 0 (no fear) to 100 (extreme fear). Ranges are inclusive of the lower bound and exclusive of the upper bound, except the last, which includes 100.00.

Figure A1

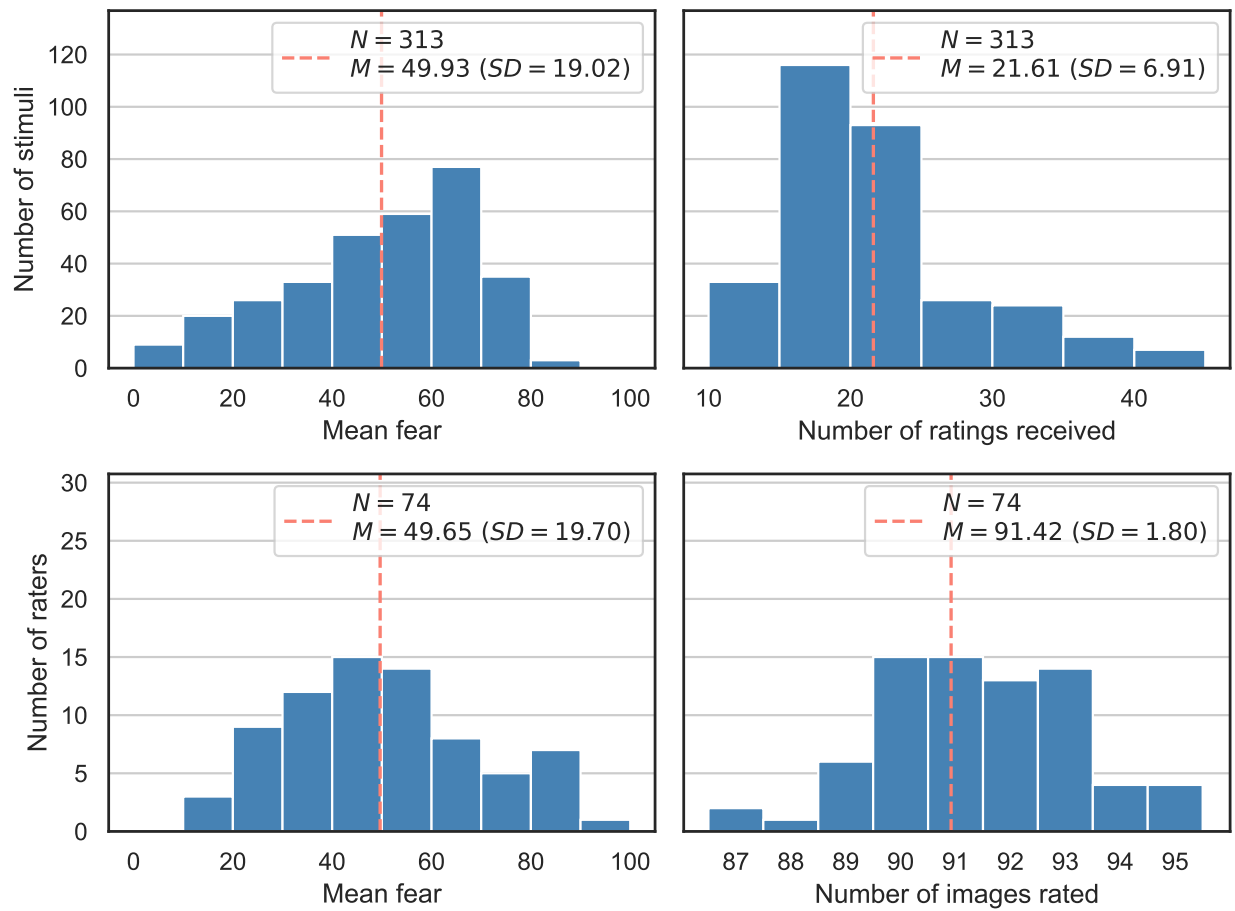
Distributions of Images and Participants Based on Mean Fear Ratings and Number of Ratings Provided



Note. The top row shows the distribution of 313 images by their mean fear ratings (left) and the number of ratings they received (right). The bottom row shows the distribution of 148 participants by their mean fear ratings (left) and the number of ratings they provided (right).

Figure A2

Distributions of Images and Participants Based on Mean Fear Ratings and Number of Ratings Provided (Group A)



Note. The top row shows the distribution of 313 images by their mean fear ratings (left) and the number of ratings they received (right). The bottom row shows the distribution of 74 participants by their mean fear ratings (left) and the number of ratings they provided (right).

Table A2*Frequency of Stimuli by Range of Mean Fear Ratings (Group A)*

Fear range	Number of stimuli	Percentage of stimuli (%)
0.00–20.00	29	9.3
20.00–40.00	59	18.8
40.00–60.00	110	35.1
60.00–80.00	112	35.8
80.00–100.00	3	1.0
Total (0–100)	313	100.0

Note. Fear scores are continuous from 0 (no fear) to 100 (extreme fear). Ranges are inclusive of the lower bound and exclusive of the upper bound, except the last, which includes 100.00.

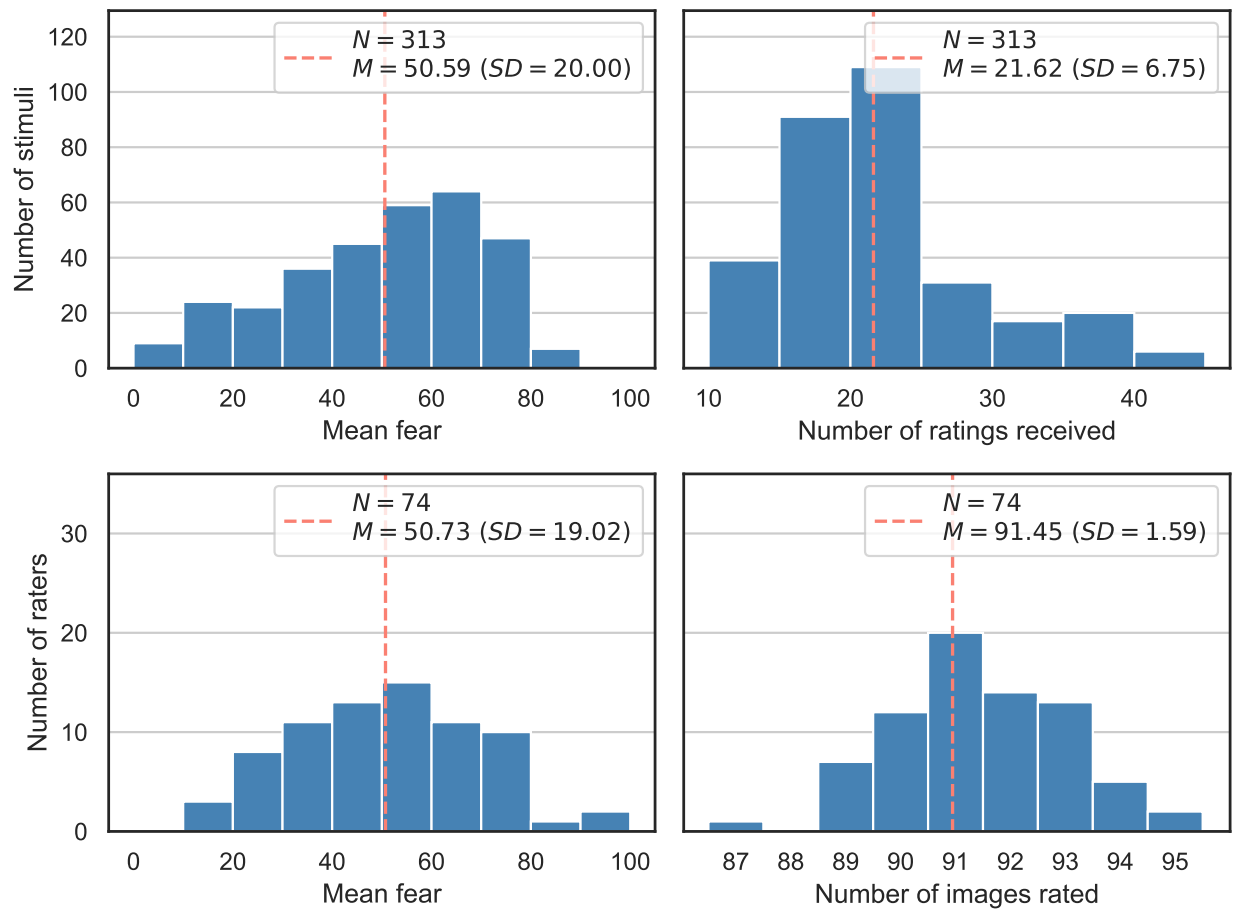
Table A3*Frequency of Stimuli by Range of Mean Fear Ratings (Group B)*

Fear range	Number of stimuli	Percentage of stimuli (%)
0.00–20.00	33	10.5
20.00–40.00	58	18.5
40.00–60.00	104	33.2
60.00–80.00	111	35.5
80.00–100.00	7	2.2
Total (0–100)	313	100.0

Note. Fear scores are continuous from 0 (no fear) to 100 (extreme fear). Ranges are inclusive of the lower bound and exclusive of the upper bound, except the last, which includes 100.00.

Figure A3

Distributions of Images and Participants Based on Mean Fear Ratings and Number of Ratings Provided (Group B)



Note. The top row shows the distribution of 313 images by their mean fear ratings (left) and the number of ratings they received (right). The bottom row shows the distribution of 74 participants by their mean fear ratings (left) and the number of ratings they provided (right).

Appendix B
Upper Bound Estimation

Table B1

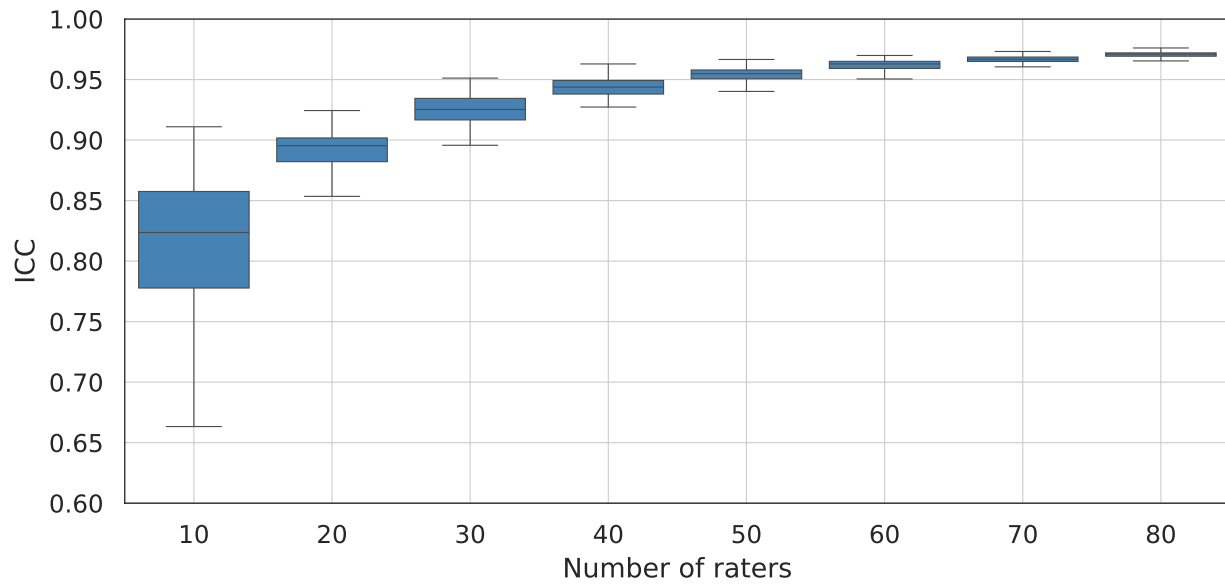
Mean (M) and standard deviation (SD) of intraclass correlation coefficient (ICC) over 100 subsampling repetitions for various subsample sizes (raters)

		Number of raters							
		10	20	30	40	50	60	70	80
ICC	M	0.813	0.890	0.925	0.944	0.954	0.962	0.967	0.971
	SD	0.058	0.021	0.013	0.008	0.005	0.004	0.003	0.003

Note. ICC = intraclass correlation coefficient.

Figure B1

Distribution of intraclass correlation coefficients (ICC) over 100 subsampling repetitions for each subsample size (raters). Boxes show the median (center line) and inter-quartile range; whiskers extend to $1.5 \times IQR$.



Appendix C

Learning Curve Analysis

Table C1*Empirical learning-curve values*

Data size	R ²			MAE			RMSE		
	ResNet	ConvNextV2	Swin	ResNet	ConvNextV2	Swin	ResNet	ConvNextV2	Swin
50	0.132	0.238	0.205	13.533	12.844	13.167	17.804	16.722	17.269
75	0.307	0.380	0.397	12.923	12.395	12.241	16.394	15.502	15.764
100	0.359	0.414	0.470	12.101	11.754	11.431	15.544	14.905	14.650
150	0.438	0.479	0.495	11.562	11.026	10.754	14.505	13.966	14.029
200	0.456	0.508	0.535	11.360	10.598	10.595	14.289	13.590	13.600
250	0.492	0.557	0.549	11.336	10.415	10.584	14.208	13.278	13.438
313	0.503	0.563	0.565	11.025	10.426	10.327	14.067	13.191	13.163

Note. MAE = Mean Absolute Error; RMSE = Root-Mean-Squared Error; R² = Coefficient of Determination.

The numbers are empirical validation scores obtained at each data set size and are the data points used to fit the learning curves in Figure 2.

Table C2*Parameters (a, b, c) of the fitted learning-curve functions*

Metric	ResNet			ConvNextV2			Swin		
	a	b	c	a	b	c	a	b	c
R ²	0.998	0.021	-0.508	0.658	0.015	-0.099	1.471	0.030	-0.927
MAE	5.461	0.016	11.093	4.865	0.011	10.188	7.185	0.019	10.398
RMSE	9.859	0.019	14.066	7.313	0.014	13.120	10.284	0.019	13.299

Note. Parameters a, b, c are those of the functions that generated the learning-curve lines in Figure 2. For error metrics (MAE, RMSE) the fitted form is an exponential decay $y(n) = a \cdot \exp(-bn) + c$. For goodness-of-fit (R^2) the fitted form is an inverse exponential $y(n) = a \cdot (1 - \exp(-bn)) + c$.

Appendix D

Grad-CAM Attributions

Figure D1

Differences in Mean Activations Between In-Mask and Out-Mask Areas Across 282 Images

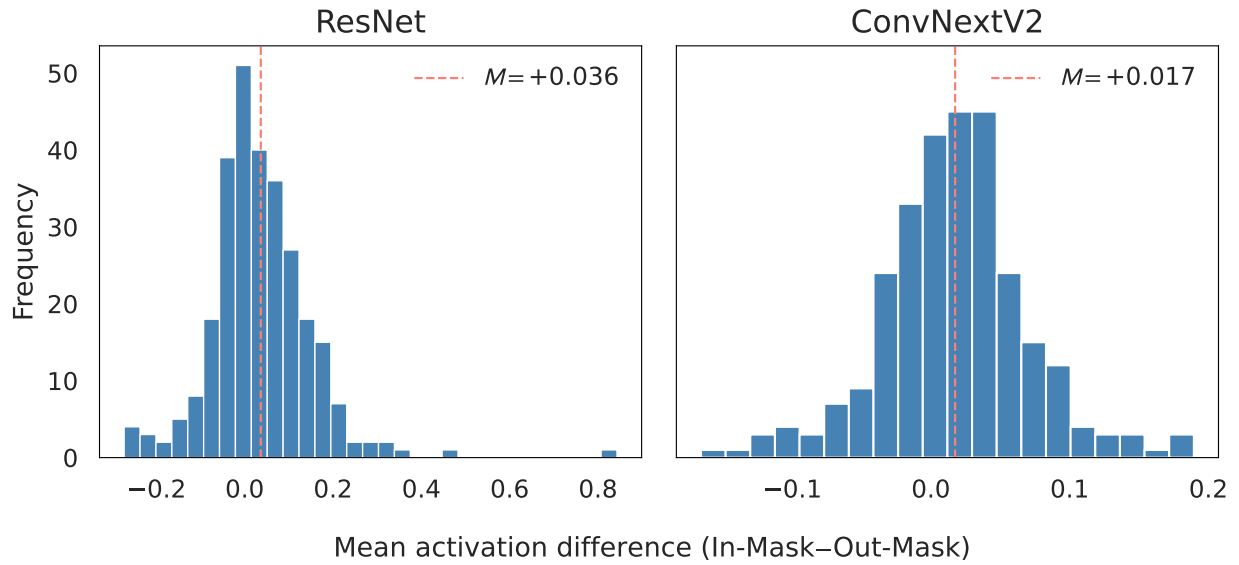


Figure D2

Mean Attributions Inside and Outside the Mask, with Corresponding Sample Sizes and t-test Results

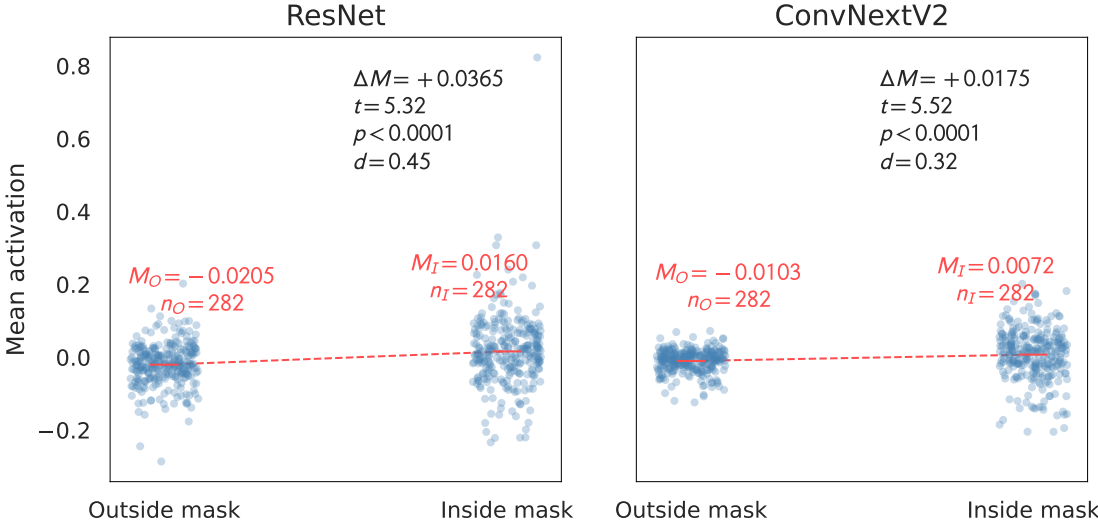
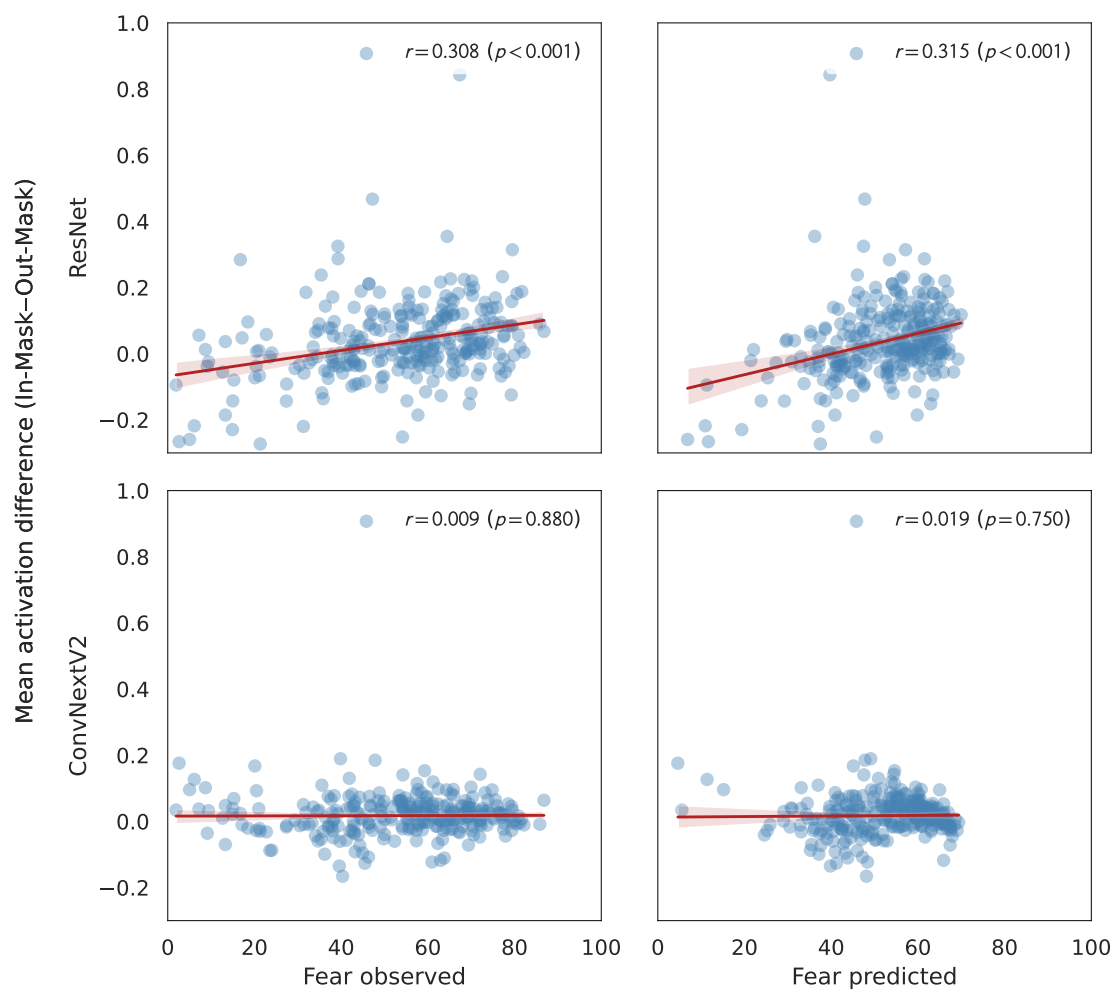


Figure D3

Correlation Between Observed/Predicted Fear Ratings and Differences in Mean Activations Between In-Mask and Out-Mask Areas (N=282 Images)



Appendix E

Feature Visualization

Methods

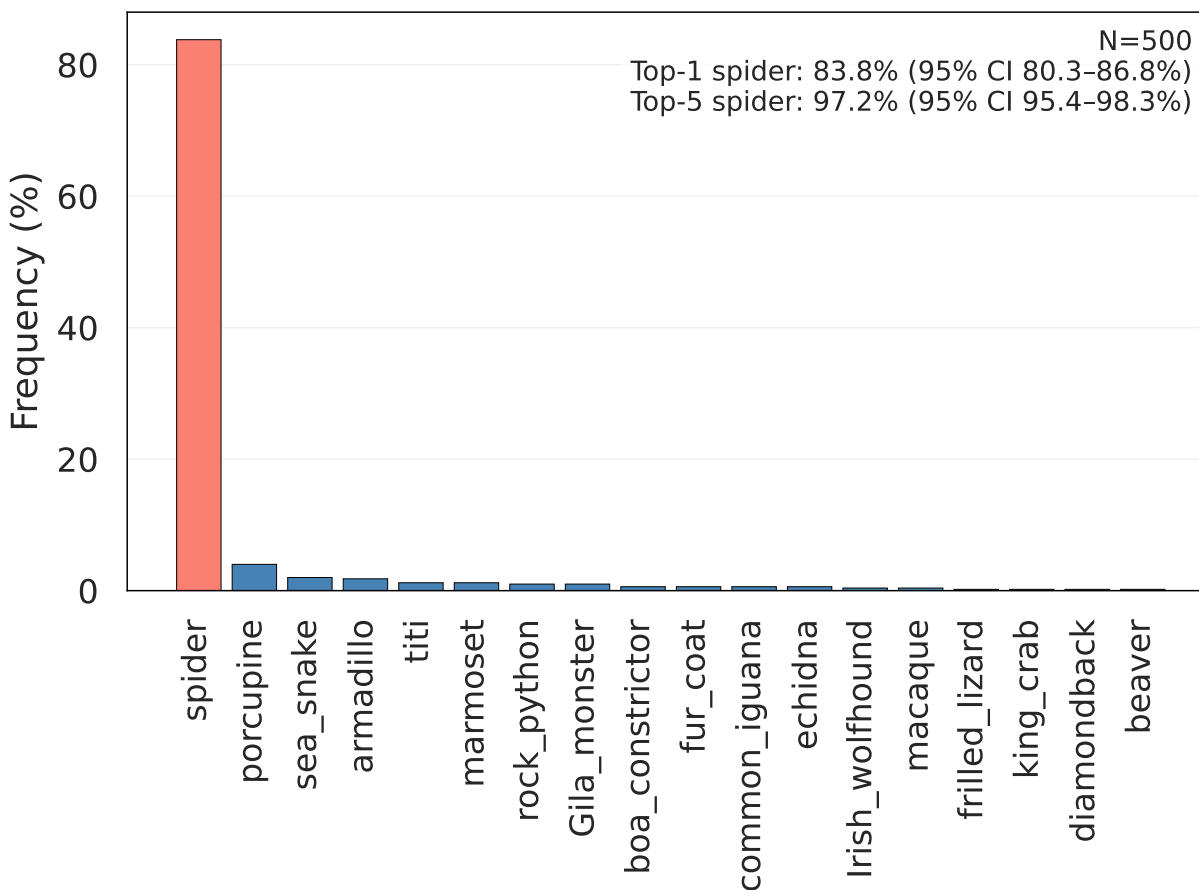
We generated feature visualizations (FVs) with torch-lucent (Kiat, 2020) to synthesize inputs that maximize the final scalar output (fear) of the task-adapted ResNet model trained on the full dataset (fully fine-tuned; lowest MAE). We used Fourier parameterization (`fft=True`) with color decorrelation (`decorrelate=True`), `sd=0.001`, and standard augmentations (`pad`, `jitter`, random scale 0.8–1.2, small rotations). Adam (`lr=0.05`; `weight_decay=1e-4`) ran for 512 steps. Identical settings applied to ConvNeXtV2 yielded high-frequency, iridescent patterns with low human interpretability; therefore, we report ResNet FVs and include ConvNeXtV2 attempts as negative results. Output clipping was disabled during FV. We generated 500 synthetic images per base model and show 9 representatives (selected by highest final activation) in Figure 4. The full set of FV outputs is available at the OSF repository.

Results – ResNet

Figure 4, E1, and E2 illustrate qualitative and quantitative FV outcomes ($N = 500$ FV images). An unadapted ResNet-ImageNet classifier assigned a spider synset (black and gold garden spider, barn spider, garden spider, black widow, tarantula, wolf spider, spider web) as top-1 for 83.8% (95% CI 80.3–86.8%) and as top-5 for 97.2% (95% CI 95.4–98.3%). The mean spider probability mass was 0.572 (95% CI 0.546–0.598). Predicted fear values from the task-adapted model (clipping disabled) had mean 157.49 ($SD = 9.41$), range 130.63–182.02. See Table E1 for a summary.

Figure E1

Predicted ImageNet-1K Classes for 500 Feature Visualizations of an Unadapted ResNet Base Model

**Table E1**

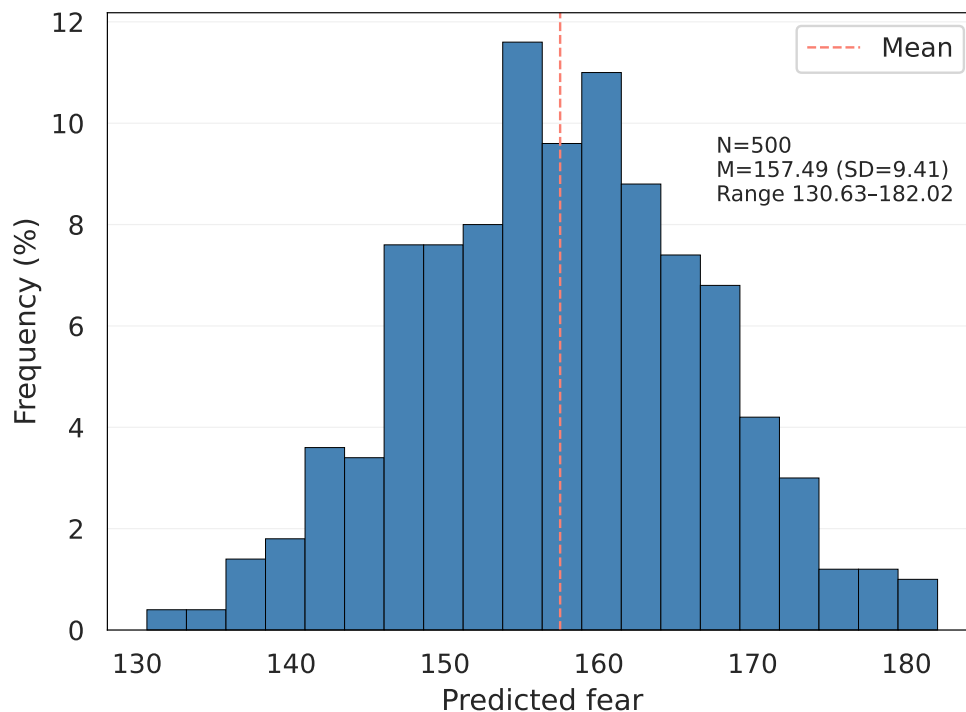
Summary of Feature Visualization Sanity Checks (N images per model)

Model	N	Spider top-1 (95% CI)	Spider top-5 (95% CI)	Spider prob. mass (mean; 95% CI)	Fear (mean \pm SD; min–max)
ResNet	500	83.8% (80.3–86.8%)	97.2% (95.4–98.3%)	0.572 (0.546–0.598)	157.49 \pm 9.41 (130.63–182.02)
ConvNeXtV2	500	13.0% (10.3–16.2%)	33.0% (29.0–37.2%)	0.064 (0.054–0.074)	101.12 \pm 7.05 (90.85–119.36)

Note. “Spider” synsets = black and gold garden spider, barn spider, garden spider, black widow, tarantula, wolf spider, spider web. Classifier = unadapted ImageNet-1K backbone with native preprocessing. Spider probability mass is the sum of softmax probabilities over the spider synsets. Task-adapted model clipping was disabled during FV.

Figure E2

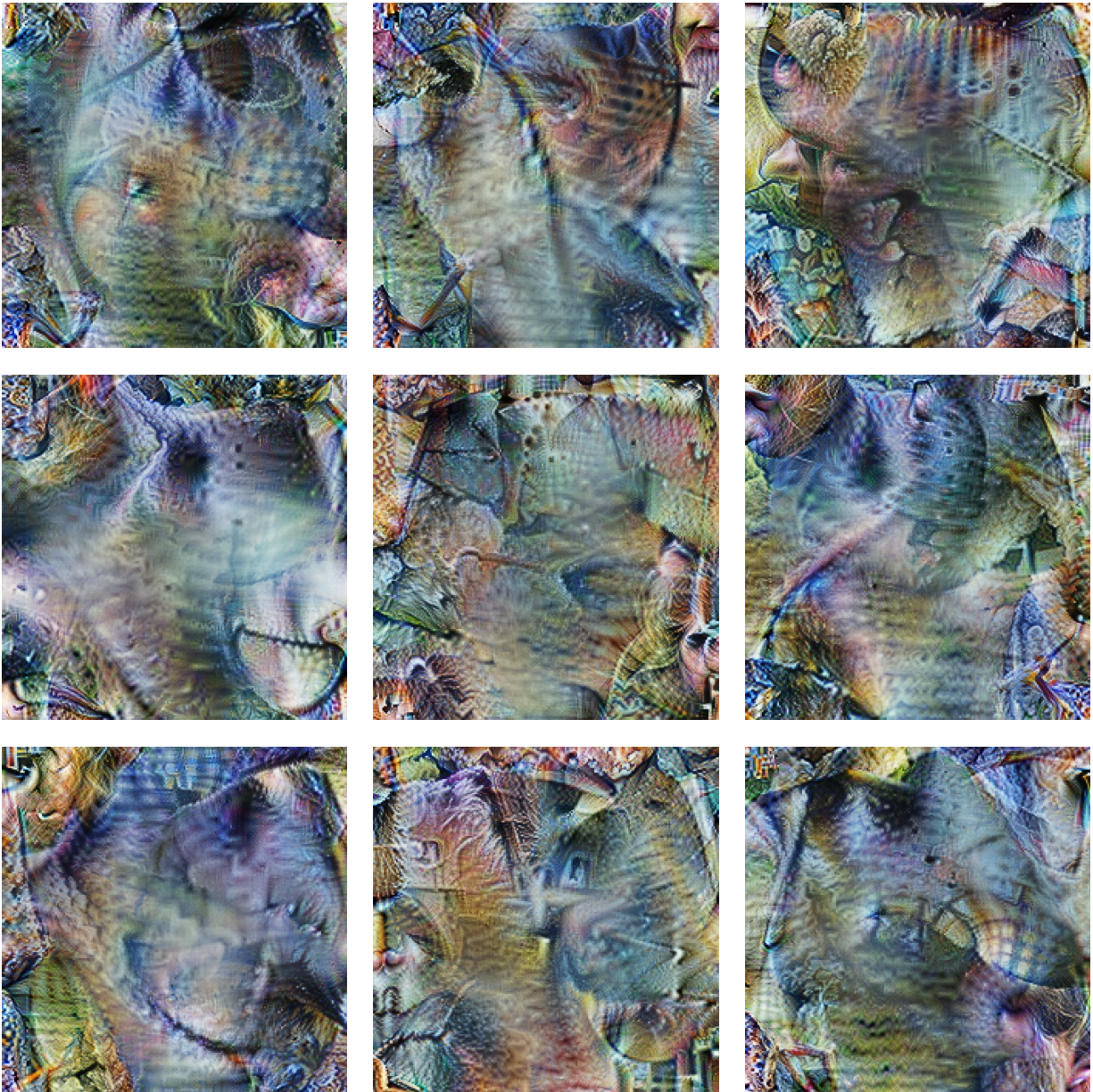
Distribution of Predicted Fear for 500 Feature Visualizations of the Task-Adapted ResNet Model

**Negative Result – ConvNeXtV2**

Under identical FV settings, ConvNeXtV2 produced iridescent patterns lacking coherent object structure ($N = 500$ images); top-1 spider 13.0% (95% CI 10.3–16.2%), top-5 spider 33.0% (95% CI 29.0–37.2%); mean spider probability mass 0.064 (95% CI 0.054–0.074). Predicted fear mean 101.12 ($SD = 7.05$), range 90.85–119.36. See Figures E4, E5 and Table E1. Examples and the full set of FV outputs are available at the OSF repository.

Figure E3

ConvNeXtV2 Feature Visualizations for the Final Output Node



Note. The figure shows nine synthetic example images that maximally activate the task-adapted model's fear rating predictions, revealing the learned features that the model associates with high fear.

Figure E4

Predicted ImageNet-1K Classes for 500 Feature Visualizations of an Unadapted ConvNeXtV2 Base Model

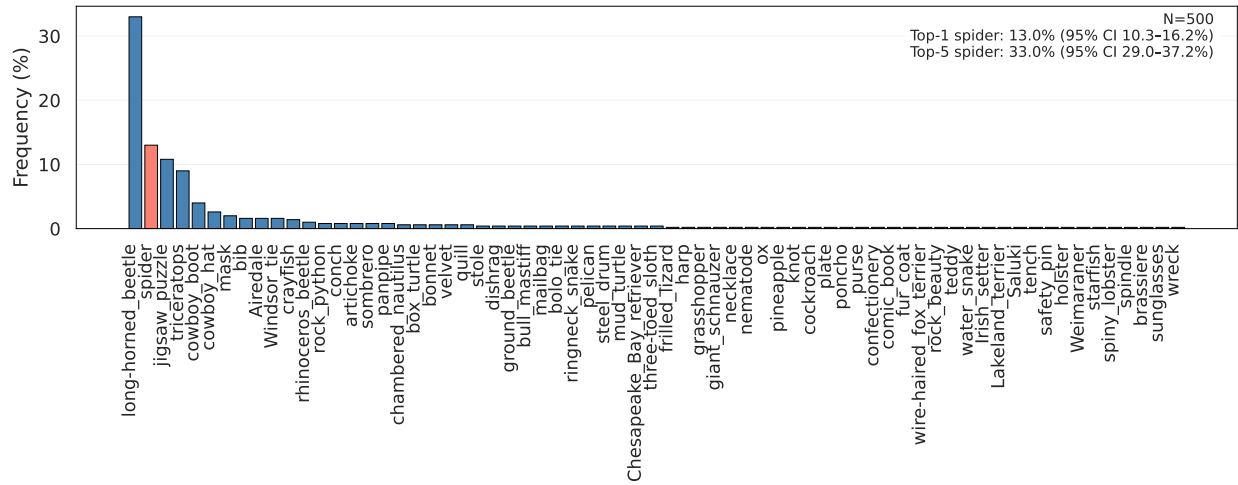
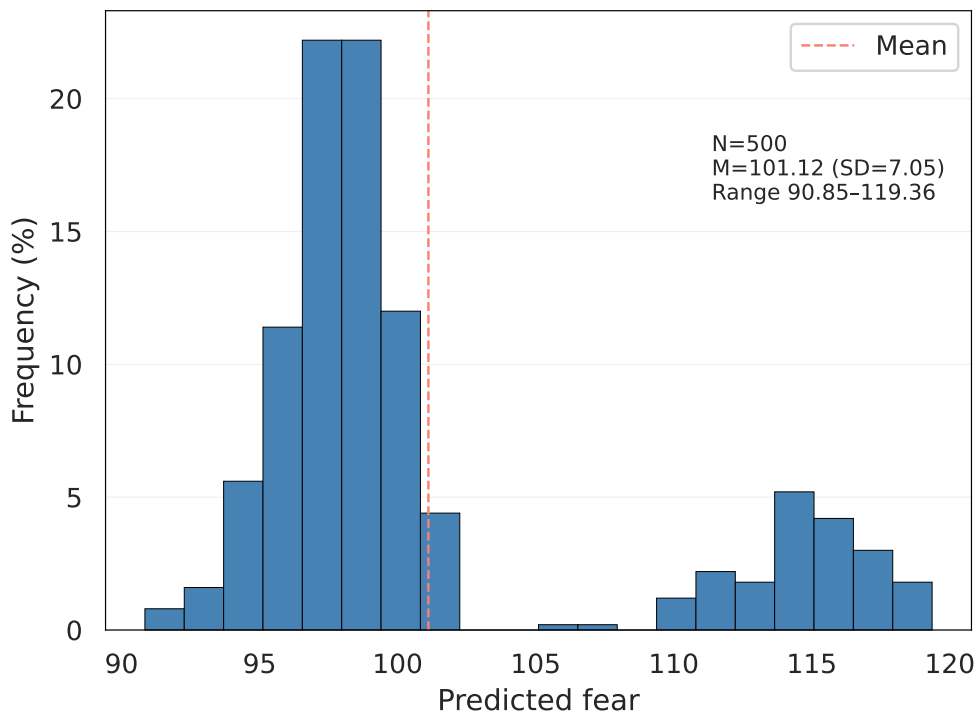


Figure E5

Distribution of Predicted Fear for 500 Feature Visualizations of the Task-Adapted ConvNeXtV2 Model



Appendix F

Error Analysis

We report complete per-criterion and per-category descriptives (n, proportion, mean/median absolute error, IQR, error share, delta) with 95% stratified bootstrap CIs for means and shares. Omnibus differences were tested with Kruskal–Wallis and FDR (Benjamini–Hochberg) across criteria; Dunn post-hoc tests (FDR within criterion) are reported where applicable. Categories with small sample sizes ($n < 10$) were summarized descriptively without inferential tests. Finally, we provide per-model figures showing error share versus category frequency across all 12 criteria.

Table F3

Dunn Post Hoc Pairwise Comparisons by Criterion for ResNet

Criterion	Category A	Category B	p (FDR)
spider in picture	artificial, painted or comic spider	no spider	0.926
spider in picture	artificial, painted or comic spider	spider	0.01
spider in picture	no spider	spider	0.009
cobweb in picture	no	yes	0.132
number of spiders	none	one spider	0.017
number of spiders	none	two or more spiders	0.159
number of spiders	one spider	two or more spiders	0.632
subjective distance	close	distant	0.0
subjective distance	close	not evaluable	0.001
subjective distance	distant	not evaluable	0.872
environment	civilization	human contact	0.514
environment	civilization	nature	0.029
environment	civilization	not evaluable	0.029
environment	human contact	nature	0.123
environment	human contact	not evaluable	0.123

Table F3 (continued) Dunn Post Hoc Pairwise Comparisons by Criterion for ResNet
/

Criterion	Category A	Category B	p (FDR)
environment	nature	not evaluable	0.573
texture	hairy	not evaluable	0.0
texture	hairy	smooth	0.051
texture	not evaluable	smooth	0.003
eyes	non-visible	not evaluable	0.027
eyes	non-visible	visible	0.187
eyes	not evaluable	visible	0.007
eating prey	eating prey	not eating prey	0.789
eating prey	eating prey	not evaluable	0.116
eating prey	not eating prey	not evaluable	0.018
subjective size	large	middle	0.194
subjective size	large	not evaluable	0.197
subjective size	large	small	0.326
subjective size	middle	not evaluable	0.035
subjective size	middle	small	0.61
subjective size	not evaluable	small	0.06
perspective	from side/front	from top/bottom	0.158
perspective	from side/front	not evaluable	0.033
perspective	from top/bottom	not evaluable	0.171
prominent legs	no	not evaluable	0.056
prominent legs	no	yes	0.056
prominent legs	not evaluable	yes	0.005

Note. Within-criterion Dunn tests with FDR (BH) adjustment applied per criterion. Columns: criterion, category_a, category_b, adjusted p-value. Shown only where omnibus tests were performed and post-hoc computation available.

Table F1

Per-Category Error Descriptives by Criterion for ResNet

Criterion	Category	n	Freq	Mean AE	SD AE	Median AE	IQR AE	Error Share	Δ (Share-Freq)	Mean CI		Share CI	
										Low	High	Low	High
spider in picture	spider	258	0.824	9.874	7.007	8.149	8.523	0.760	-0.064	9.067	10.696	0.724	0.794
spider in picture	artificial, painted or comic spider	26	0.083	15.968	11.799	11.749	13.781	0.124	0.041	11.816	20.481	0.094	0.155
spider in picture	no spider	29	0.093	13.422	6.780	13.338	9.565	0.116	0.023	10.963	16.021	0.096	0.137
cobweb in picture	no	198	0.633	11.148	7.887	9.260	8.832	0.659	0.026	10.032	12.180	0.621	0.691
cobweb in picture	yes	115	0.367	9.953	7.340	7.902	8.742	0.341	-0.026	8.624	11.304	0.309	0.379
number of spiders	one spider	259	0.827	10.412	7.845	8.302	8.685	0.805	-0.023	9.494	11.368	0.777	0.830
number of spiders	none	29	0.093	13.422	6.780	13.338	9.565	0.116	0.023	11.049	15.805	0.096	0.137
number of spiders	two or more spiders	25	0.080	10.639	6.756	8.877	9.680	0.079	-0.001	8.331	13.241	0.063	0.099
subjective distance	close	223	0.712	9.461	7.268	7.676	7.825	0.629	-0.083	8.588	10.458	0.595	0.669
subjective distance	distant	59	0.188	14.135	8.535	12.860	12.843	0.249	0.060	12.003	16.257	0.217	0.280
subjective distance	not evaluable	31	0.099	13.168	6.631	13.000	9.123	0.122	0.023	10.892	15.422	0.102	0.143
environment	nature	162	0.518	9.584	6.151	7.951	8.580	0.463	-0.054	8.642	10.542	0.427	0.500
environment	civilization	53	0.169	14.444	11.162	10.302	12.668	0.228	0.059	11.817	17.395	0.193	0.268
environment	human contact	53	0.169	11.617	7.193	10.803	9.573	0.184	0.014	9.754	13.686	0.157	0.212
environment	not evaluable	45	0.144	9.293	7.005	7.606	7.944	0.125	-0.019	7.414	11.392	0.100	0.151
texture	smooth	126	0.403	11.175	8.171	9.139	9.576	0.420	0.018	9.765	12.613	0.378	0.460
texture	hairy	145	0.463	9.152	6.751	7.704	7.438	0.396	-0.067	8.005	10.342	0.358	0.433
texture	not evaluable	42	0.134	14.686	7.881	13.511	10.288	0.184	0.050	12.333	17.214	0.156	0.213
eyes	non-visible	178	0.569	10.801	7.517	8.990	9.087	0.574	0.005	9.759	11.953	0.535	0.615
eyes	visible	106	0.339	9.813	8.112	7.930	7.389	0.310	-0.028	8.325	11.429	0.272	0.348
eyes	not evaluable	29	0.093	13.422	6.780	13.338	9.565	0.116	0.023	11.049	15.777	0.097	0.136
eating prey	not eating prey	259	0.827	10.509	7.974	8.273	8.828	0.812	-0.015	9.498	11.464	0.789	0.835
eating prey	not evaluable	29	0.093	13.422	6.780	13.338	9.565	0.116	0.023	10.832	15.803	0.095	0.137
eating prey	eating prey	25	0.080	9.636	4.807	9.469	7.224	0.072	-0.008	7.913	11.550	0.059	0.087
subjective size	middle	104	0.332	10.034	8.548	8.043	8.064	0.311	-0.021	8.482	11.708	0.274	0.354
subjective size	large	88	0.281	11.500	8.017	9.134	10.833	0.302	0.021	9.910	13.290	0.266	0.339
subjective size	small	87	0.278	9.914	6.504	8.001	8.162	0.257	-0.021	8.583	11.369	0.229	0.289
subjective size	not evaluable	34	0.109	12.761	6.610	12.818	8.825	0.129	0.021	10.552	15.144	0.107	0.151
perspective	from side/front	162	0.518	9.777	6.999	7.722	8.457	0.473	-0.045	8.724	10.925	0.433	0.513
perspective	from top/bottom	112	0.358	11.523	8.836	9.283	8.641	0.385	0.027	9.934	13.131	0.346	0.425
perspective	not evaluable	39	0.125	12.246	6.563	11.819	8.261	0.142	0.018	10.084	14.254	0.120	0.166
color of picture	color	304	0.971	10.671	7.760	8.644	9.178	0.968	-0.003	9.795	11.494	0.958	0.976
color of picture	(black/white)	9	0.029	12.000	5.417	12.527	4.050	0.032	0.003	8.938	15.506	0.024	0.042
prominent legs	no	133	0.425	11.254	7.963	9.158	8.939	0.447	0.022	9.950	12.647	0.407	0.484
prominent legs	yes	151	0.482	9.708	7.500	7.641	8.665	0.437	-0.045	8.527	10.916	0.398	0.477
prominent legs	not evaluable	29	0.093	13.422	6.780	13.338	9.565	0.116	0.023	11.076	15.873	0.097	0.137

Note. For each criterion/category: n , frequency of images, mean/median absolute error, IQR, contribution to total absolute error

(error share; sums to 1 within a criterion), and over/under-representation (Δ =share-freq). 95% CIs are provided for mean and share.

Small- n categories should be interpreted cautiously.

Table F2*Category-Wise Omnibus Tests by Criterion for ResNet*

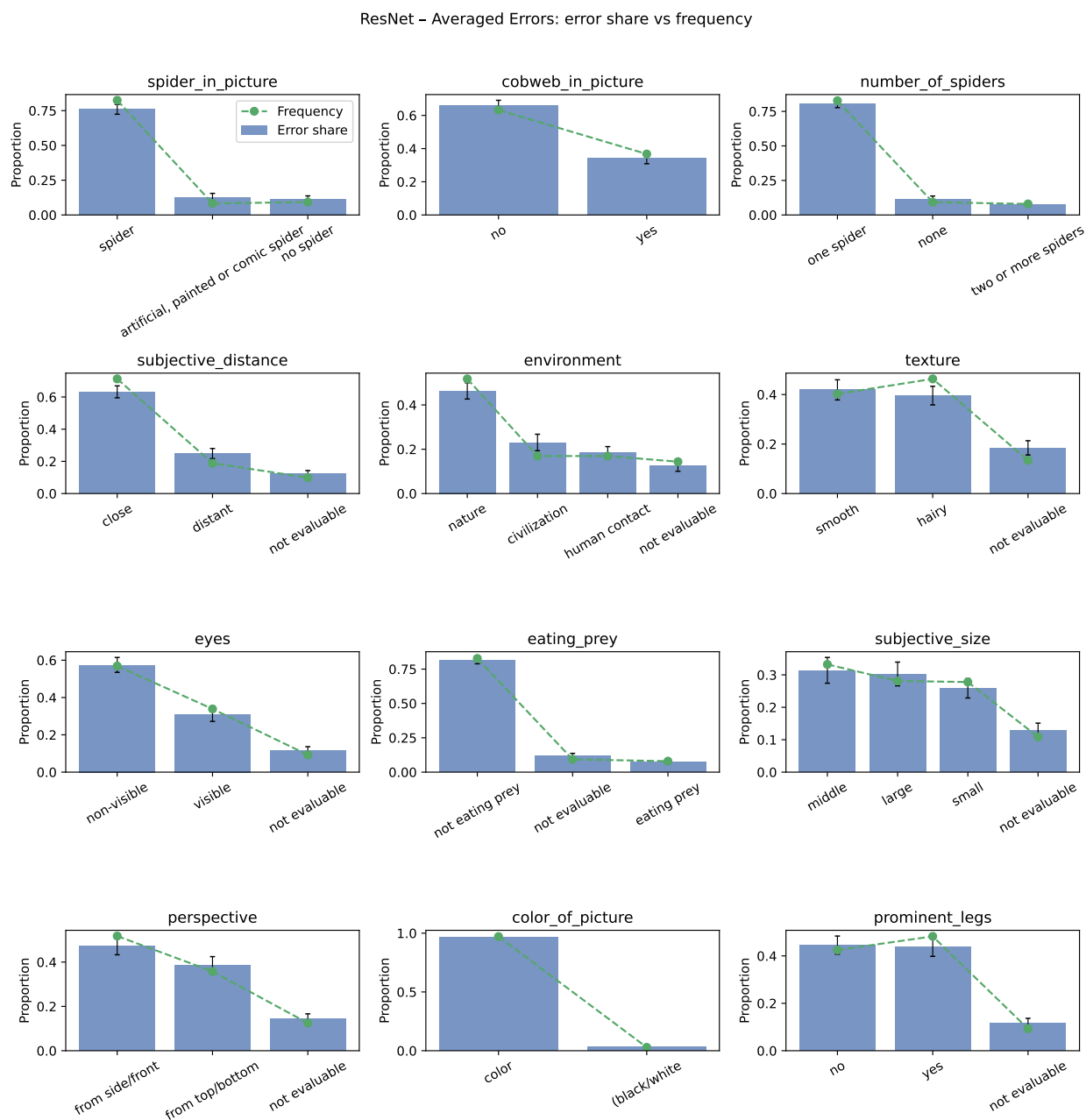
Criterion	H	ϵ^2	p	p (FDR)	Significant (FDR)	N	k	Reason
spider in picture	14.856	0.041	<0.001	0.002	True	313	3	
cobweb in picture	2.266	0.004	0.132	0.132	False	313	2	
number of spiders	7.701	0.018	0.021	0.031	True	313	3	
subjective distance	24.349	0.072	<0.001	<0.001	True	313	3	
environment	10.695	0.025	0.013	0.025	True	313	4	
texture	20.156	0.059	<0.001	<0.001	True	313	3	
eyes	9.217	0.023	0.010	0.022	True	313	3	
eating prey	7.544	0.018	0.023	0.031	True	313	3	
subjective size	8.866	0.019	0.031	0.034	True	313	4	
perspective	7.364	0.017	0.025	0.031	True	313	3	
color of picture					True	313	2	small cells (min_n=10)
prominent legs	11.139	0.029	0.004	0.010	True	313	3	

Note. Kruskal–Wallis tests across categories within each criterion. Epsilon-squared (ϵ^2) reported as effect size.

FDR-adjusted p -values (Benjamini–Hochberg) across criteria; 'significant_FDR' indicates adjusted $p < 0.05$. Criteria with small cells ($n < \text{threshold}$) are not tested.

Figure F1

Error Share Versus Category Frequency Across All Criteria for ResNet



Note. Each panel shows one criterion; bars are categories. Blue bar height = category’s share of total absolute error (sums to 1 within a panel). Black caps denote 95% stratified bootstrap CIs. Dashed line with markers = category frequency (proportion of images; also sums to 1). Bar > dashed line indicates over-representation in error ($\Delta > 0$); bar < dashed line indicates under-representation. Errors for the best-performing configuration of ResNet. Categories with small n may have wide CIs; ‘not evaluatable’ levels are included where present.

Table F6*Dunn Post Hoc Pairwise Comparisons by Criterion for ConvNeXtV2*

Criterion	Category A	Category B	p (FDR)
spider in picture	artificial, painted or comic spider	no spider	0.091
spider in picture	artificial, painted or comic spider	spider	0.0
spider in picture	no spider	spider	0.091
cobweb in picture	no	yes	0.021
number of spiders	none	one spider	0.531
number of spiders	none	two or more spiders	0.711
number of spiders	one spider	two or more spiders	0.742
subjective distance	close	distant	0.044
subjective distance	close	not evaluable	0.044
subjective distance	distant	not evaluable	0.74
environment	civilization	human contact	0.419
environment	civilization	nature	0.11
environment	civilization	not evaluable	0.419
environment	human contact	nature	0.419
environment	human contact	not evaluable	0.876
environment	nature	not evaluable	0.419
texture	hairy	not evaluable	0.003
texture	hairy	smooth	0.057
texture	not evaluable	smooth	0.069
eyes	non-visible	not evaluable	0.382
eyes	non-visible	visible	0.8
eyes	not evaluable	visible	0.382
eating prey	eating prey	not eating prey	0.603
eating prey	eating prey	not evaluable	0.306

Table F6
 (continued) Dunn Post Hoc Pairwise Comparisons by Criterion for ConvNeXtV2
 /

Criterion	Category A	Category B	p (FDR)
eating prey	not eating prey	not evaluable	0.306
subjective size	large	middle	0.236
subjective size	large	not evaluable	0.952
subjective size	large	small	0.238
subjective size	middle	not evaluable	0.238
subjective size	middle	small	0.798
subjective size	not evaluable	small	0.331
perspective	from side/front	from top/bottom	0.923
perspective	from side/front	not evaluable	0.529
perspective	from top/bottom	not evaluable	0.529
prominent legs	no	not evaluable	0.395
prominent legs	no	yes	0.276
prominent legs	not evaluable	yes	0.276

Note. Within-criterion Dunn tests with FDR (BH) adjustment applied per criterion. Columns: criterion, category_a, category_b, adjusted p-value. Shown only where omnibus tests were performed and post-hoc computation available.

Table F4

Per-Category Error Descriptives by Criterion for ComuNeXtV2

Criterion	Category	n	Freq	Mean AE	SD AE	Median AE	IQR AE	Error Share	Δ (Share-Freq)	Mean CI		Share CI	
										Low	High	Low	High
spider in picture	spider	258	0.824	9.576	6.230	8.599	7.500	0.761	-0.063	8.823	10.329	0.730	0.790
spider in picture	artificial, painted or comic spider	26	0.083	17.236	10.510	15.730	15.219	0.138	0.055	13.576	21.093	0.111	0.167
spider in picture	no spider	29	0.093	11.248	5.888	10.393	6.450	0.101	0.008	9.211	13.247	0.083	0.119
cobweb in picture	no	198	0.633	10.929	7.021	9.514	8.304	0.667	0.034	9.913	11.830	0.630	0.699
cobweb in picture	yes	115	0.367	9.400	6.777	8.300	7.024	0.333	-0.034	8.226	10.730	0.301	0.370
number of spiders	one spider	259	0.827	10.201	6.987	8.787	7.551	0.814	-0.013	9.422	11.074	0.785	0.839
number of spiders	none	29	0.093	11.248	5.888	10.393	6.450	0.101	0.008	9.308	13.384	0.083	0.120
number of spiders	two or more spiders	25	0.080	11.070	7.925	9.881	12.309	0.085	0.005	8.072	14.426	0.063	0.108
subjective distance	close	223	0.712	9.566	6.375	8.616	7.182	0.657	-0.055	8.800	10.468	0.624	0.692
subjective distance	distant	59	0.188	12.587	8.704	11.210	11.896	0.229	0.040	10.582	14.765	0.197	0.260
subjective distance	not evaluable	31	0.099	11.911	6.304	10.668	9.132	0.114	0.015	9.786	14.044	0.095	0.135
environment	nature	162	0.518	9.309	5.673	8.619	6.885	0.465	-0.053	8.437	10.164	0.430	0.501
environment	civilization	53	0.169	13.320	9.895	10.723	12.018	0.218	0.048	10.855	15.923	0.183	0.254
environment	human contact	53	0.169	10.065	5.740	10.112	8.178	0.164	-0.005	8.592	11.586	0.143	0.188
environment	not evaluable	45	0.144	11.056	7.480	8.787	8.276	0.153	0.010	8.961	13.278	0.126	0.182
texture	smooth	126	0.403	11.198	7.907	9.098	8.322	0.435	0.032	9.866	12.580	0.396	0.474
texture	hairy	145	0.463	8.795	5.104	7.664	7.251	0.393	-0.070	7.953	9.666	0.362	0.429
texture	not evaluable	42	0.134	13.304	8.179	11.024	11.082	0.172	0.038	10.948	15.869	0.145	0.202
eyes	non-visible	178	0.569	10.373	7.290	8.602	8.563	0.569	0.000	9.345	11.492	0.534	0.606
eyes	visible	106	0.339	10.117	6.697	8.973	7.713	0.330	-0.008	8.907	11.343	0.297	0.366
eyes	not evaluable	29	0.093	11.248	5.888	10.393	6.450	0.101	0.008	9.091	13.431	0.082	0.120
eating prey	not eating prey	259	0.827	10.397	7.223	8.787	8.489	0.830	0.002	9.483	11.230	0.805	0.850
eating prey	not evaluable	29	0.093	11.248	5.888	10.393	6.450	0.101	0.008	9.243	13.450	0.083	0.120
eating prey	eating prey	25	0.080	9.040	5.077	9.005	3.984	0.070	-0.010	7.244	11.251	0.056	0.085
subjective size	middle	104	0.332	9.751	7.477	8.515	7.537	0.312	-0.020	8.375	11.207	0.277	0.350
subjective size	large	88	0.281	11.241	6.759	10.201	9.157	0.305	0.024	9.884	12.680	0.274	0.338
subjective size	small	87	0.278	9.972	6.812	8.583	7.275	0.267	-0.011	8.508	11.460	0.235	0.302
subjective size	not evaluable	34	0.109	11.064	6.167	9.755	6.608	0.116	0.007	9.093	13.257	0.095	0.137
perspective	from side/front	162	0.518	9.927	6.037	8.907	6.974	0.496	-0.022	8.990	10.867	0.459	0.533
perspective	from top/bottom	112	0.358	10.873	8.428	8.674	9.292	0.375	0.017	9.346	12.446	0.338	0.413
perspective	not evaluable	39	0.125	10.749	5.847	10.393	6.577	0.129	0.005	8.872	12.668	0.110	0.153
color of picture	color	304	0.971	10.305	6.978	8.804	8.133	0.965	-0.006	9.516	11.127	0.954	0.976
color of picture	(black/white)	9	0.029	12.495	6.315	11.540	3.098	0.035	0.006	8.867	16.609	0.024	0.046
prominent legs	no	133	0.425	11.098	8.027	9.340	8.601	0.455	0.030	9.810	12.509	0.420	0.492
prominent legs	yes	151	0.482	9.555	6.026	8.377	7.637	0.445	-0.038	8.584	10.464	0.409	0.478
prominent legs	not evaluable	29	0.093	11.248	5.888	10.393	6.450	0.101	0.008	9.251	13.193	0.083	0.119

Note. For each criterion/category: n , frequency of images, mean/median absolute error, IQR, contribution to total absolute error (error share; sums to 1 within a criterion), and over/under-representation (Δ =share-freq). 95% CIs are provided for mean and share. Small- n categories should be interpreted cautiously.

Table F5*Category-Wise Omnibus Tests by Criterion for ConvNeXtV2*

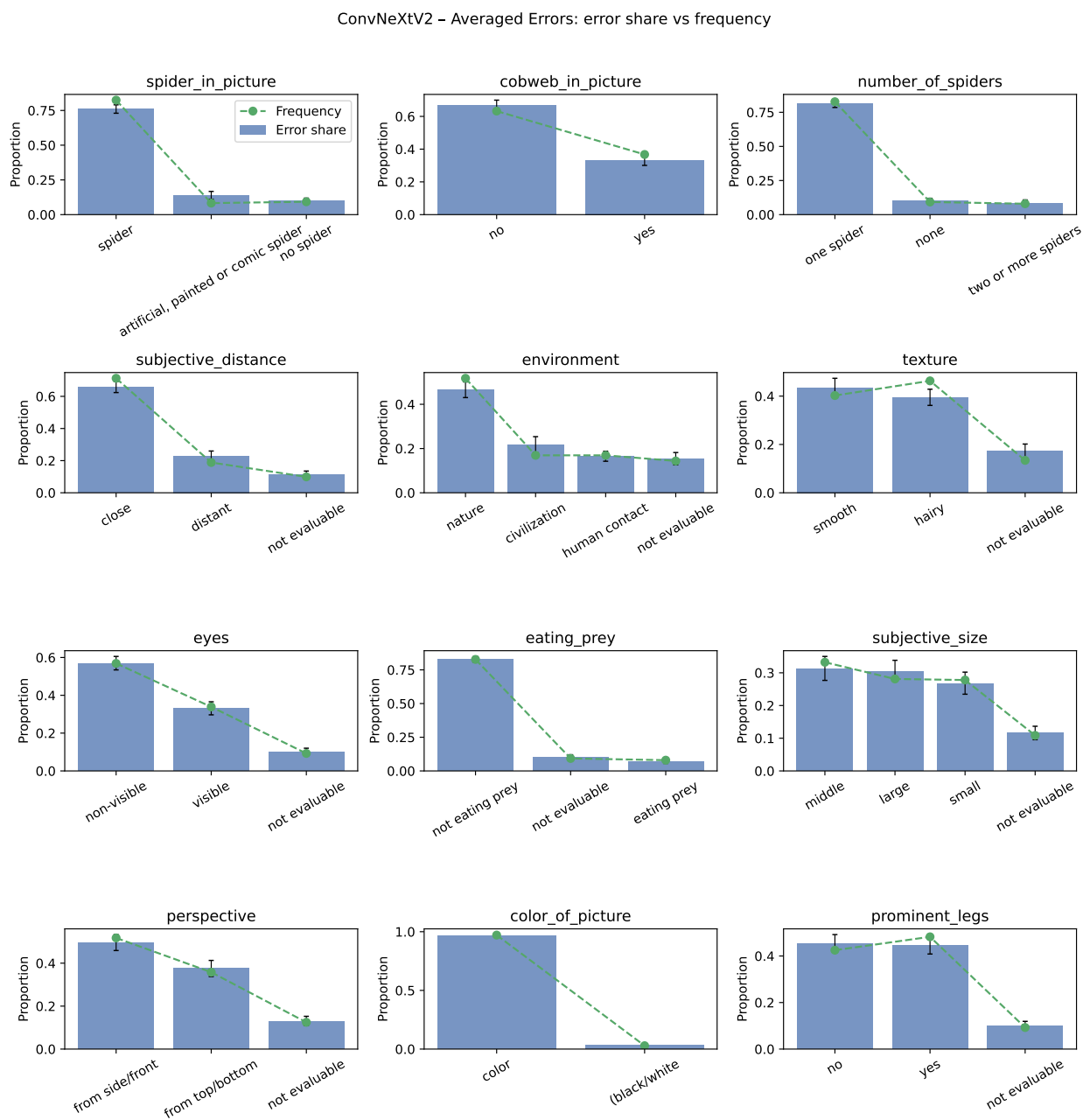
Criterion	H	ϵ^2	p	p (FDR)	Significant (FDR)	N	k	Reason
spider in picture	16.876	0.048	<0.001	0.002	True	313	3	
cobweb in picture	5.306	0.014	0.021	0.058	False	313	2	
number of spiders	1.863	0.000	0.394	0.443	False	313	3	
subjective distance	8.871	0.022	0.012	0.043	True	313	3	
environment	5.951	0.010	0.114	0.228	False	313	4	
texture	11.988	0.032	0.002	0.014	True	313	3	
eyes	1.819	-0.001	0.403	0.443	False	313	3	
eating prey	2.026	0.000	0.363	0.443	False	313	3	
subjective size	5.750	0.009	0.124	0.228	False	313	4	
perspective	1.003	-0.003	0.606	0.606	False	313	3	
color of picture					True	313	2	small cells (min_n=10)
prominent legs	3.520	0.005	0.172	0.270	False	313	3	

Note. Kruskal-Wallis tests across categories within each criterion. Epsilon-squared (ϵ^2) reported as effect size.

FDR-adjusted p -values (Benjamini-Hochberg) across criteria; 'significant_FDR' indicates adjusted $p < 0.05$. Criteria with small cells ($n < \text{threshold}$) are not tested.

Figure F2

Error Share Versus Category Frequency Across All Criteria for ConvNeXtV2



Note. Each panel shows one criterion; bars are categories. Blue bar height = category’s share of total absolute error (sums to 1 within a panel). Black caps denote 95% stratified bootstrap CIs. Dashed line with markers = category frequency (proportion of images; also sums to 1). Bar > dashed line indicates over-representation in error ($\Delta > 0$); bar < dashed line indicates under-representation. Errors for the best-performing configuration of ConvNeXtV2. Categories with small n may have wide CIs; ‘not evaluable’ levels are included where present.

Table F9*Dunn Post Hoc Pairwise Comparisons by Criterion for Swin*

Criterion	Category A	Category B	p (FDR)
spider in picture	artificial, painted or comic spider	no spider	0.444
spider in picture	artificial, painted or comic spider	spider	0.033
spider in picture	no spider	spider	0.16
cobweb in picture	no	yes	0.206
number of spiders	none	one spider	0.484
number of spiders	none	two or more spiders	0.69
number of spiders	one spider	two or more spiders	0.728
subjective distance	close	distant	0.001
subjective distance	close	not evaluable	0.206
subjective distance	distant	not evaluable	0.282
environment	civilization	human contact	0.031
environment	civilization	nature	0.002
environment	civilization	not evaluable	0.031
environment	human contact	nature	0.746
environment	human contact	not evaluable	0.997
environment	nature	not evaluable	0.746
texture	hairy	not evaluable	0.011
texture	hairy	smooth	0.09
texture	not evaluable	smooth	0.09
eyes	non-visible	not evaluable	0.331
eyes	non-visible	visible	0.621
eyes	not evaluable	visible	0.331
eating prey	eating prey	not eating prey	0.935
eating prey	eating prey	not evaluable	0.533

Table F9 (continued) Dunn Post Hoc Pairwise Comparisons by Criterion for Swin
/

Criterion	Category A	Category B	p (FDR)
eating prey	not eating prey	not evaluable	0.507
subjective size	large	middle	0.432
subjective size	large	not evaluable	0.82
subjective size	large	small	0.432
subjective size	middle	not evaluable	0.432
subjective size	middle	small	0.936
subjective size	not evaluable	small	0.432
perspective	from side/front	from top/bottom	0.304
perspective	from side/front	not evaluable	0.304
perspective	from top/bottom	not evaluable	0.727
prominent legs	no	not evaluable	0.352
prominent legs	no	yes	0.699
prominent legs	not evaluable	yes	0.352

Note. Within-criterion Dunn tests with FDR (BH) adjustment applied per criterion. Columns: criterion, category_a, category_b, adjusted p-value. Shown only where omnibus tests were performed and post-hoc computation available.

Table F7

Per-Category Error Descriptives by Criterion for Swin

Criterion	Category	n	Freq	Mean AE	SD AE	Median AE	IQR AE	Error Share	Δ (Share-Freq)	Mean CI		Share CI		Share CI High
										Low	High	Low	High	
spider in picture	spider	258	0.824	9.359	6.184	7.611	8.846	0.764	-0.061	8.632	10.155	0.726	0.797	
spider in picture	artificial, painted or comic spider	26	0.083	15.801	12.023	12.465	20.335	0.130	0.047	11.630	20.294	0.098	0.161	
spider in picture	no spider	29	0.093	11.626	7.682	9.388	6.841	0.107	0.014	9.156	14.269	0.085	0.129	
cobweb in picture	no	198	0.633	10.461	7.232	8.373	9.616	0.655	0.022	9.431	11.374	0.617	0.689	
cobweb in picture	yes	115	0.367	9.491	7.119	7.451	6.858	0.345	-0.022	8.268	10.874	0.311	0.383	
number of spiders	one spider	259	0.827	9.859	7.017	7.922	8.879	0.807	-0.020	9.036	10.706	0.774	0.838	
number of spiders	none	25	0.093	11.626	7.682	9.388	6.841	0.107	0.014	9.089	14.443	0.084	0.131	
number of spiders	two or more spiders	25	0.080	10.886	8.405	8.178	9.836	0.086	0.006	7.810	14.248	0.063	0.112	
subjective distance	close	223	0.712	9.258	6.823	7.490	7.852	0.653	-0.060	8.434	10.228	0.617	0.690	
subjective distance	distant	59	0.188	12.765	7.692	12.789	9.732	0.238	0.050	10.779	14.587	0.206	0.269	
subjective distance	not evaluable	31	0.099	11.130	7.685	8.794	7.077	0.109	0.010	8.566	13.942	0.084	0.134	
environment	nature	162	0.518	8.923	5.667	7.550	7.379	0.457	-0.061	8.018	9.807	0.420	0.493	
environment	civilization	53	0.169	14.400	10.003	12.789	11.073	0.241	0.072	11.974	17.116	0.206	0.280	
environment	human contact	53	0.169	9.736	6.696	7.633	8.865	0.163	-0.006	8.105	11.544	0.138	0.192	
environment	not evaluable	45	0.144	9.733	7.114	7.774	7.847	0.138	-0.005	7.787	11.850	0.112	0.167	
texture	smooth	126	0.403	10.756	8.069	8.307	9.964	0.429	0.026	9.315	12.090	0.385	0.469	
texture	hairy	145	0.463	8.812	5.791	7.443	7.507	0.404	-0.059	7.862	9.824	0.369	0.443	
texture	not evaluable	42	0.134	12.612	7.995	9.940	7.795	0.167	0.033	10.331	15.053	0.139	0.197	
eyes	non-visible	178	0.569	10.115	7.060	7.868	9.906	0.569	0.001	9.142	11.184	0.534	0.610	
eyes	visible	106	0.339	9.671	7.293	7.923	7.818	0.324	-0.015	8.343	10.930	0.285	0.358	
eyes	not evaluable	29	0.093	11.626	7.682	9.388	6.841	0.107	0.014	9.007	14.596	0.083	0.132	
eating prey	not eating prey	259	0.827	10.027	7.333	7.774	9.111	0.821	-0.006	9.078	10.838	0.793	0.847	
eating prey	not evaluable	29	0.093	11.626	7.682	9.388	6.841	0.107	0.014	9.045	14.496	0.085	0.132	
eating prey	eating prey	25	0.080	9.145	4.709	8.506	6.430	0.072	-0.008	7.374	11.101	0.059	0.088	
subjective size	middle	104	0.332	9.785	7.480	7.442	9.051	0.322	-0.011	8.486	11.338	0.287	0.362	
subjective size	large	88	0.281	10.779	7.429	9.524	9.481	0.300	0.019	9.293	12.335	0.267	0.337	
subjective size	small	87	0.278	9.443	6.553	7.451	7.700	0.260	-0.018	8.132	10.904	0.229	0.295	
subjective size	not evaluable	34	0.109	11.028	7.330	8.580	6.585	0.119	0.010	8.800	13.534	0.095	0.143	
perspective	from side/front	162	0.518	9.446	6.576	7.703	8.350	0.484	-0.034	8.450	10.523	0.445	0.527	
perspective	from top/bottom	112	0.358	10.810	7.982	8.596	9.503	0.383	0.025	9.391	12.368	0.345	0.421	
perspective	not evaluable	39	0.125	10.814	7.195	8.461	7.294	0.133	0.009	8.676	13.161	0.109	0.161	
color of picture	color	304	0.971	10.152	7.270	8.076	9.146	0.976	0.005	9.382	10.959	0.969	0.983	
color of picture	(black/white)	9	0.029	8.491	3.734	8.333	3.801	0.024	-0.005	6.123	10.785	0.017	0.031	
prominent legs	yes	151	0.482	9.574	6.312	7.922	8.883	0.457	-0.025	8.542	10.580	0.417	0.495	
prominent legs	no	133	0.425	10.375	7.977	7.924	9.067	0.436	0.011	9.099	11.747	0.397	0.475	
prominent legs	not evaluable	29	0.093	11.626	7.682	9.388	6.841	0.107	0.014	9.111	14.425	0.084	0.131	

Note. For each criterion/category: n , frequency of images, mean/median absolute error, IQR, contribution to total absolute error (error share; sums to 1 within a criterion), and over/under-representation (Δ =share-freq). 95% CIs are provided for mean and share. Small- n categories should be interpreted cautiously.

Table F8*Category-Wise Omnibus Tests by Criterion for Swin*

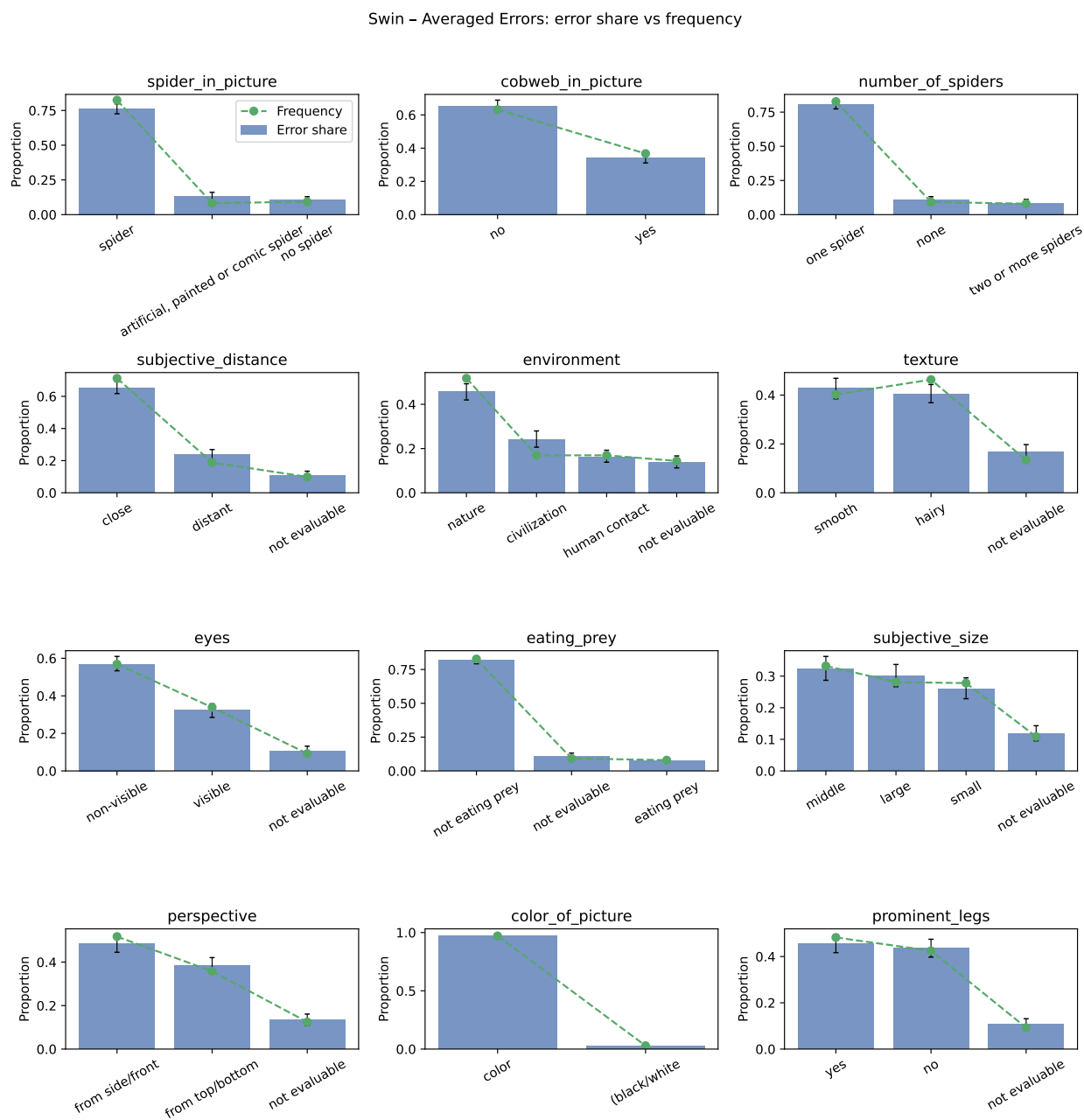
Criterion	H	ϵ^2	p	p (FDR)	Significant (FDR)	N	k	Reason
spider in picture	8.332	0.020	0.016	0.043	True	313	3	
cobweb in picture	1.602	0.002	0.206	0.426	False	313	2	
number of spiders	2.010	0.000	0.366	0.426	False	313	3	
subjective distance	13.636	0.038	0.001	0.012	True	313	3	
environment	13.318	0.033	0.004	0.022	True	313	4	
texture	9.058	0.023	0.011	0.040	True	313	3	
eyes	2.133	0.000	0.344	0.426	False	313	3	
eating prey	1.895	0.000	0.388	0.426	False	313	3	
subjective size	2.642	-0.001	0.450	0.450	False	313	4	
perspective	2.626	0.002	0.269	0.426	False	313	3	
color of picture					True	313	2	small cells (min_n=10)
prominent legs	2.038	0.000	0.361	0.426	False	313	3	

Note. Kruskal–Wallis tests across categories within each criterion. Epsilon-squared (ϵ^2) reported as effect size.

FDR-adjusted p -values (Benjamini–Hochberg) across criteria; 'significant_FDR' indicates adjusted $p < 0.05$. Criteria with small cells ($n < \text{threshold}$) are not tested.

Figure F3

Error Share Versus Category Frequency Across All Criteria for Swin



Note. Each panel shows one criterion; bars are categories. Blue bar height = category’s share of total absolute error (sums to 1 within a panel). Black caps denote 95% stratified bootstrap CIs. Dashed line with markers = category frequency (proportion of images; also sums to 1). Bar > dashed line indicates over-representation in error ($\Delta > 0$); bar < dashed line indicates under-representation. Errors for the best-performing configuration of Swin. Categories with small n may have wide CIs; ‘not evaluatable’ levels are included where present.